nanomaterials

MDPI

Article

Entropy Generation and Statistical Analysis of MHD Hybrid Nanofluid Unsteady Squeezing Flow between Two Parallel Rotating Plates with Activation Energy

Nimer Murshid [1,*], Hasan Mulki [1,*], Mahmoud Abu-Samha [1], Wahib Owhaib [2], S. Suresh Kumar Raju [3], Chakravarthula S. K. Raju [4], Macherla JayachandraBabu [5], Raad Z. Homod [6] and Wael Al-Kouz [1,*]

1 College of Engineering and Technology, American University of the Middle East, Kuwait; mahmoud.abusamha@aum.edu.kw
2 Mechanical and Maintenance Engineering Department, German Jordanian University, Amman 11180, Jordan; wahib.owhaib@gju.edu.jo
3 Department of Mathematics and Statistics, College of Science, King Faisal University, P.O. Box 400, Al-Ahsa 31982, Saudi Arabia; ssurapuraju@kfu.edu.sa
4 Department of Mathematics, GITAM School of Science, GITAM Deemed to be University, Bangalore 562163, India; rchakrav@gitam.edu
5 Department of Mathematics, S.V.A Government College, Srikalahasti 517644, India; jayamacharla@gmail.com
6 Department of Oil and Gas Engineering, Basrah University for Oil and Gas, Basrah 61004, Iraq; raadahmood@yahoo.com
* Correspondence: nimer.murshid@aum.edu.kw (N.M.); hasan.mulki@aum.edu.kw (H.M.); wael.kouz@aum.edu.kw (W.A.-K.)

Citation: Murshid, N.; Mulki, H.; Abu-Samha, M.; Owhaib, W.; Raju, S.S.K.; Raju, C.S.K.; JayachandraBabu, M.; Homod, R.Z.; Al-Kouz, W. Entropy Generation and Statistical Analysis of MHD Hybrid Nanofluid Unsteady Squeezing Flow between Two Parallel Rotating Plates with Activation Energy. *Nanomaterials* **2022**, *12*, 2381. https://doi.org/10.3390/nano12142381

Academic Editors: Taseer Muhammad and Metib Alghamdi

Received: 19 June 2022
Accepted: 8 July 2022
Published: 12 July 2022

Abstract: Squeezing flow is a flow where the material is squeezed out or disfigured within two parallel plates. Such flow is beneficial in various fields, for instance, in welding engineering and rheometry. The current study investigates the squeezing flow of a hybrid nanofluid (propylene glycol–water mixture combined with paraffin wax–sand) between two parallel plates with activation energy and entropy generation. The governing equations are converted into ordinary differential equations using appropriate similarity transformations. The shooting strategy (combined with Runge–Kutta fourth order method) is applied to solve these transformed equations. The results of the conducted parametric study are explained and revealed in graphs. This study uses a statistical tool (correlation coefficient) to illustrate the impact of the relevant parameters on the engineering parameters of interest, such as the surface friction factor at both plates. This study concludes that the squeezing number intensifies the velocity profiles, and the rotating parameter decreases the fluid velocity. In addition, the magnetic field, rotation parameter, and nanoparticle volumetric parameter have a strong negative relationship with the friction factor at the lower plate. Furthermore, heat source has a strong negative relationship with heat transfer rate near the lower plate, and a strong positive correlation with the same phenomena near the upper plate. In conclusion, the current study reveals that the entropy generation is increased with the Brinkman number and reduced with the squeezing parameter. Moreover, the results of the current study verify and show a decent agreement with the data from earlier published research outcomes.

Keywords: squeezing flow; parallel plates; hybrid nanofluid; activation energy; correlation coefficient; entropy generation; hybrid nanomaterials

1. Introduction

Squeezing flow is defined as a flow where the material is squeezed out or disfigured in two parallel plates. The flow is useful in various fields, for instance, in welding engineering and rheometry. In addition, utilizing nanofluids in various industrial applications is extensively investigated for augmented heat transfer characteristics. Squeeze flow is an attractive technique for measuring the rheological properties of materials that create

difficulties in conventional rheometers, for example, very viscous materials, fluids with an apparent yield stress, fluids that tend to slip at instrument walls, or materials with large particles (these characteristics often appear together) (Engmann et al. [1]). Su and Yin [2] analyzed the squeezing flow of the fluid among parallel plates with an inclined magnetic field, and witnessed the reduction in the fluid temperature with a larger squeezing number. In addition, Munawar et al. [3] applied a shooting strategy to unriddle the system of equations in their analysis of rotating and squeezed flow amidst parallel plates and discovered that, near the boundaries, a larger magnetic field parameter ameliorates the pressure gradient. Shahmohamadi and Rashidi [4] used the variational iteration (VI) method to provide analytical solutions in the investigation of various nanofluid flows amidst parallel plates, and noticed that the addition of nanoparticles to the fluid exhibits a prominent influence on its velocity. Hayat et al. [5] attempted to investigate the effect of nonlinear radiation on MHD flow over a stretching cylinder. In addition, Khan et al. [6] explicated the characteristics of heat transfer in the water-based nanofluid rotating flow where the solutions are offered by the Runge–Kutta–Fehlberg method. With the assistance of a finite difference scheme, Ahmad et al. [7] numerically scrutinized the nanofluid flow amidst parallel plates with Brownian motion and thermophoresis. They remarked that the fluid velocity is minified with a larger porosity parameter. Al-Kouz et al. [8,9] numerically investigated the rarified nanofluid flow inside a square cavity with fins, and inside a pipe. In addition, Al-Kouz et al. [10] provided an entropy generation optimization study of nanofluids inside a cavity. Moreover, Mahanthesh et al. [11] examined the effect of radiation on nanoliquid flow over a vertical plate. Furthermore, Alshare et al. [12] provided the effect of the wavy configuration module on the flow of nanofluids. Owhaib et al. [13] presented a 3D numerical analysis of rotating nanofluid flow radiation and viscous heating effect using the modified Buongiorno model. Al-Kouz and Owhaib [14] investigated Casson nanofluid heat transfer characteristics over a rotating frame. Atlas et al. [15] studied unsteady Casson nanofluid flow amidst parallel plates with Cattaneo–Christov heat flux. Tarakaramu and Narayana [16] elucidated rotating bioconvective fluid flow among parallel plates with chemical reactions, and observe that the Brownian motion lowers the motile density distribution. Alzahrani et al. [17] examined squeezed flow among parallel plates with cross-diffusion effects, and discovered that the squeezing parameter meliorates fluid temperature. In addition, Khan et al. [18] analyzed the entropy generation optimization in the squeezing flow of second-grade fluid among two parallel plates with thermophoresis and Brownian motion. They emphasized that there is an escalation in the entropy generation with the raise in squeezing parameter. Upreti et al. [19] discussed the optimization of entropy generation in the squeezing flow of hybrid nanofluid with a magnetic field. Zangooee et al. and Salehi et al. [20,21] used the Akbari–Ganji method (AGM) to numerically study various nanofluid rotating flows amidst parallel plates, and acknowledge that the skin friction minifies with a larger Eckert number. Awan et al. [22] employed the Adams P–C method together with R–K4th to solve the mathematical model of the EMHD micropolar fluid flow among parallel plates with Hall current. In addition, Shankar et al. [23] examined the temperature profile in two cases i.e., Fourier's law model and non-Fourier's law model (C–C heat flux), and detected that there is a diminution in temperature when the latter is incorporated compared to the former. Magodora et al. [24] applied the spectral quasi-linearization (SQ) method to scrutinize the radiative rotating flow of nanofluid amidst parallel plates with the non-Fourier's law model, and observed that the nanoparticle volume fraction parameter minimizes the Sherwood number. Recently, Mollah et al. [25] elucidated the rotating flow of Bingham fluid amidst parallel plates with Hall current, and discovered that the velocity profile slowly achieves a steady-state compared with the temperature profile. It is worth mentioning that no study reported in the literature that performs irreversibility analysis in the squeezing flow of hybrid nanofluid between two parallel plates with activation energy and thermal radiation.

Nanofluids were developed as a novel type of heat transfer fluid that may be used in lieu of conventional fluids in industrial operations. They are used in a variety of appli-

cations, including refrigeration, heat exchangers, and electronic device cooling. Hybrid nanoparticles are defined as nanoparticles composed of two or more different materials of nanometer size. The fluids prepared with hybrid nanoparticles are known as hybrid nanofluids. Generally, a hybrid nanofluid (HNF) is a superior alternative to a nanofluid (NF). For illustration, silver and copper have more noteworthy thermal conductivities, yet they are flimsy and chemically reactive. By performing the hybridization of such nanoparticles with ceramic or metal oxides, the ensuring HNF shows more prominent rheological behavior and thermo-physical attributes, alongside the developed heat transfer features (Babu et al. [26]). HNF is utilized in various heat transfer applications admitting micropower generation and solar thermal systems. A hybrid nanofluid, which is a combination of a propylene glycol–water mixture and paraffin wax–sand, may be utilized as a standby for the propylene glycol–water blend in the solar thermal framework. Hayat et al. [27] used the shooting method to obtain the results of a study of the ferromagnetic nanomaterial fluid flow of Maxwell fluid on a stretching surface with a magnetic dipole effect. They noticed an improvement in fluid temperature as the ferromagnetic interaction variable increased. The results of Chen et al. [28,29] indicate that the scattering effect, including the scattering ability and scattering phase function, is significant to evaluate the direct solar absorption performance of nanoparticle suspensions, and Cu@C nanoparticle suspensions can be a potential working fluid in solar thermal conversion applications. Furthermore, Qayyum et al. [30] considered different water-based nanofluid flows with Ohmic heating and slip effect, using a rotating disc with variable thickness as a geometry. Their findings include the observation that as the stretching parameter improves, the fluid velocity increases. Moreover, Waini et al. [31] elucidated the nixed convective flow of a water-based hybrid nanofluid using a thin needle and remarked that, near the lower branch, a larger volume fraction nanoparticle of copper ameliorates the temperature. Later, several researchers [32–34] considered different stretching surfaces, and analyzed fluid flow with various parameters including radiation and magnetic field. They discovered that the Eckert number and non-linear parameter meliorate fluid temperature. In addition, Khan et al. [35] used Cattaneo–Christov double diffusions to simulate the slip flow of Williamson nanofluid on a permeable stretching surface. One of their findings is that the Williamson parameter can help reduce shear stress. Acharya et al. [36] noticed that the Hall current parameter ameliorates the heat transport in the examination of the radiative flow through a spinning disk. In addition, Eid and Nafe [37] elucidated the flow via an exponentially shrinking/stretching sheet with a heat sink/source. They observed that along with shrinking sheet, copper and magnetite volume fraction nanoparticle parameters exhibit different behaviors on the velocity profile. Also, Khan et al. [38] investigated the non-Darcy flow of micropolar ferrofluid on a permeable stretching sheet in the slip regime using Joule heating and heat generation/absorption. They discovered that the micropolar parameter increases fluid velocity. Abbas et al. [39] numerically simulated hybrid nanofluid (SWCNT–MWCNT/water) flow with bvp4c strategy for two models, Xue and Yamada–Ota, through a thin needle. Ahmad and Nadeem [40] discussed entropy generation optimization in Casson–EG/(SWCNT–MWCNT) fluid flow through a lubricated surface, and detected that the Casson parameter shows mixed behavior on the entropy generation profile. Recently, many authors [41–44] considered stretching surface and rotating disk, and numerically investigated different hybrid nanofluid flows with various parameters, including Arrhenius energy.

Initially, Menzinger and Wolfgang [44] deliberated the conceptual meaning of Arrhenius activation energy. In addition, Khan et al. [45] used HAM to investigate the effect of chemical reactions on tangent hyperbolic fluid flow on a slender stretching surface with a heat source/sink. They detected a decrease in fluid concentration for larger chemical reaction parameters. Moreover, Devi and Mabood [46] concluded that the activation energy parameter minimizes the Sherwood number in the scrutiny of entropy generation minimization (EGM) on the Maxwell fluid flow through a rotating disk with the Marangoni model. Furthermore, Kumar et al. [47] explained the features of heat transfer in the tangent

hyperbolic fluid flow on an elongated sheet with activation energy and thermophoresis. In addition, Bhatti and Michaelides [48] used Mathematica software to offer numerical solutions to the bioconvective nanofluid flow on a Riga plate, and observed a diminution in fluid concentration with a larger reaction rate parameter. Khan and Alzahrani [49] inspected the entropy generation optimization in the dissipative flow of Jeffrey nanofluid on a curved stretched surface with thermophoresis and activation energy. In addition, Irfan et al. [50] explained the characteristics of the mass flux concept with activation energy on the blended convective flow of Carreau fluid. Also, Wang et al. [51] investigated the effect of homogeneous and heterogeneous reactions on the dissipative flow of an Oldroyd-B fluid over a convectively heated surface with a heat source/sink. They discovered that increasing the heterogeneous parameter improves fluid concentration. Recently, many researchers [52–55] considered different geometries and demonstrated various fluid flows with activation energy, and detected that the Reynolds number minimizes the tangential velocity.

The modeling of rotating flow is critically important across a wide range of scientific, engineering, and product design applications, providing design capability for products such as jet engines, pumps, and vacuum cleaners, and modeling capability for geophysical flows. Even for applications where rotation is not initially evident, the subject is often fundamental to understanding and modeling the details of the flow physics. Examples include the vorticity produced in flow along a channel, the secondary flow produced for flow around a bend, and the wing-tip vortices produced downstream of a wing [56]. Hayat et al. [57] found that the temperature profile increases by increasing the rotation parameter in their analysis on the rotating flow of an $Ag - CuO/H_2O$ hybrid nanofluid with radiation and partial slip boundary effects. Shoaib et al. [58] numerically investigated the rotating flow of hybrid nanofluid over a stretchable sheet with thermal radiation, and noticed a reduction in the velocity field with the rise in rotation parameter. Recently, Lie et al. [59] and Mohd Sohut et al. [60] discussed the rotating flows of various hybrid nanofluids over a stretching sheet under different conditions. In addition to the previously mentioned references, more work related to nanofluids and nanogeometries can be found in [61–63].

It is noticed that no study found in the literature was conducted on the unsteady radiative squeezing flow of hybrid nanofluid between two parallel plates with irreversibility analysis. Hence, the current paper's objective is to investigate such flow with a propylene glycol–water-based hybrid nanofluid with viscous dissipation. The Arrhenius energy equation is integrated to explain mass transport phenomena. Impressions of diverse parameters on the flow are demonstrated by expending tables and graphs. Results are verified with the earlier outcomes, and an acceptable accord is noticed. The main goal of this research is to provide answers to the following related research questions:

1. How important is the activation energy in binary nanofluid flow versus mono nanofluid flow?
2. What effect does the thermal radiation parameter have on the binary hybrid nanofluid flow when positive and negative squeezing numbers are taken into account?
3. What effect does the Brinkmann number have on entropy generation in two cases, binary and mono nanofluid flows?
4. Is the reduction of shear stress near the surface is an important task in fluid flow problems?
5. Is the magnetic field parameter relevant to this phenomenon?

2. Formulation

We considered an incompressible, unsteady, three-dimensional squeezing flow of a hybrid nanofluid amidst (two) parallel plates. We took propylene glycol–water mixture as a base fluid and paraffin wax and sand as nanomaterials, and exhibited the values of their thermophysical attributes in Table 1. Presumptions for the formulation are:

- Higher plate is positioned at $y = h(t)$ and lower plate is placed at $y = 0$, where $h(t) = \sqrt{\frac{(1-\gamma t)v_f}{a}}$;

- Lower plate is elongated with the velocity $u_w = \frac{ax}{1-\gamma t}$.;
- Magnetic field of intensiveness $B(t) = \frac{B_0}{\sqrt{1-\gamma t}}$ is applied normal to the flow (see Figure 1);
- Squeezing velocity and angular velocity of the fluid are $V_h = \frac{dh}{dt}$ and $\Omega* = \frac{\omega}{1-\gamma t}$;
- T_w and T_h are the temperatures of lower and upper plates, respectively;
- Nanoparticles and base fluid are supposed to be in equilibrium. and no-slip arises amongst them;
- Neglected induced magnetic field and Joule heating.

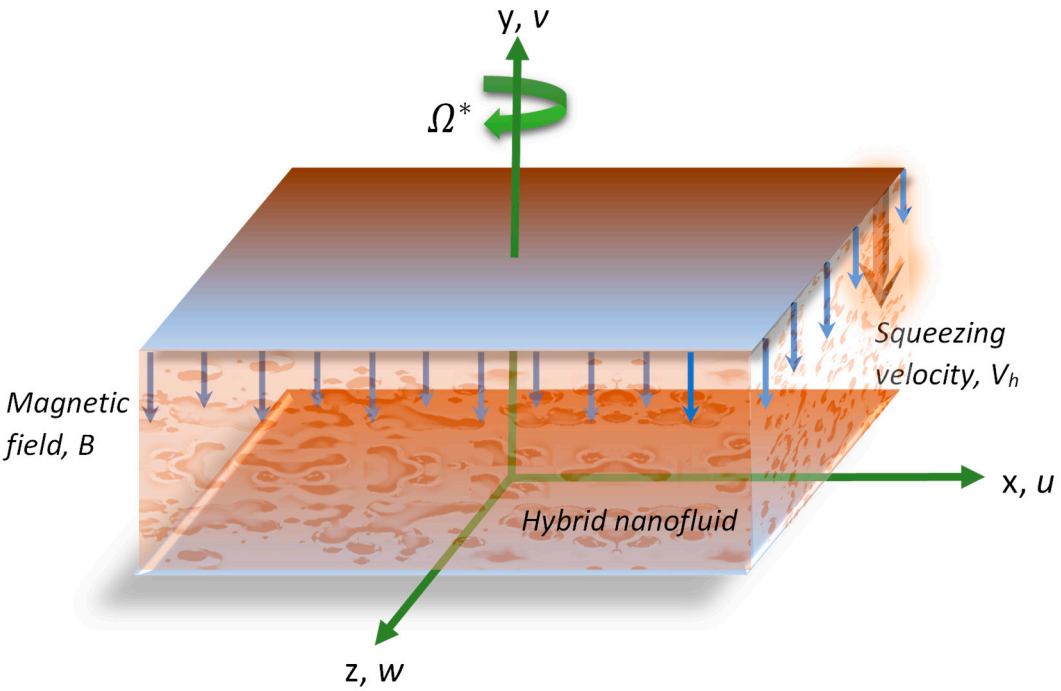

Figure 1. Flow illustration of hybrid nanofluid among two rotating parallel plates.

With these premises, the conservation of mass Equation (1), conservation of momentum Equations (2)–(4), conservation of energy Equation (5), and diffusion Equation (6) are given as (Munawar et al. [3], Alzahrani et al. [17], Anantha Kumar et al. [64], and Irfan et al. [50], respectively):

$$\frac{\partial u}{\partial x} + \frac{\partial v}{\partial y} = 0 \tag{1}$$

$$\frac{\partial u}{\partial t} + u\frac{\partial u}{\partial x} + v\frac{\partial u}{\partial y} + \frac{2\omega}{1-\gamma t}w = -\frac{1}{\rho_{hnf}}\frac{\partial p}{\partial x} + \upsilon_{hnf}\left(\frac{\partial^2 u}{\partial x^2} + \frac{\partial^2 u}{\partial y^2}\right) - \frac{\sigma B^2(t)}{\rho_{hnf}}u \tag{2}$$

$$\frac{\partial v}{\partial t} + u\frac{\partial v}{\partial x} + v\frac{\partial v}{\partial y} = -\frac{1}{\rho_{hnf}}\frac{\partial p}{\partial y} + \upsilon_{hnf}\left(\frac{\partial^2 v}{\partial x^2} + \frac{\partial^2 v}{\partial y^2}\right) \tag{3}$$

$$\frac{\partial w}{\partial t} + u\frac{\partial w}{\partial x} + v\frac{\partial w}{\partial y} - \frac{2\omega}{1-\gamma t}u = \upsilon_{hnf}\left(\frac{\partial^2 w}{\partial x^2} + \frac{\partial^2 w}{\partial y^2}\right) - \frac{\sigma B^2(t)}{\rho_{hnf}}w \tag{4}$$

$$\begin{aligned}\frac{\partial T}{\partial t} + u\frac{\partial T}{\partial x} + v\frac{\partial T}{\partial y} &= \frac{k_{hnf}}{(\rho C_p)_{hnf}}\left(\frac{\partial^2 T}{\partial x^2} + \frac{\partial^2 T}{\partial y^2}\right) - \frac{1}{(\rho C_p)_{hnf}}\frac{\partial q_r}{\partial y} \\ &+ \frac{Q_0}{(\rho C_p)_{hnf}}(T - T_h)\end{aligned} \tag{5}$$

$$\frac{\partial C}{\partial t} + u\frac{\partial C}{\partial x} + v\frac{\partial C}{\partial y} = D_m\left(\frac{\partial^2 C}{\partial x^2} + \frac{\partial^2 C}{\partial y^2}\right) - k_r\left(\frac{T}{T_h}\right)^n Exp\left(-\frac{E_a}{k_1 T}\right)(C - C_h) \tag{6}$$

With the boundary conditions (Khan et al. [6]):

$$\left.\begin{array}{l} u = u_w, v = -\frac{-V_0}{1-\gamma t}, w = 0, T = T_w, C = C_w \; at \; y = 0 \\ u = 0, v = V_h = \frac{dh}{dt}, w = 0, T = T_h, C = C_h \; at \; y = h(t) \end{array}\right\} \tag{7}$$

In Equation (5), q_r is taken to examine the heat transport performance and it can be defined as:

$$q_r = -\frac{4\sigma*}{3k*}\left(\frac{\partial^2}{\partial x^2} + \frac{\partial^2}{\partial y^2}\right)T^4 \tag{8}$$

The Taylor series expansion of T^4 in terms of T_h is (after ignoring higher order terms):

$$T^4 \approx 4T_h^3 T - 3T_h^4 \tag{9}$$

Using (8) and (9), Equation (5) can be rewritten as:

$$\frac{\partial T}{\partial t} + u\frac{\partial T}{\partial x} + v\frac{\partial T}{\partial y} = \frac{k_{hnf}}{(\rho C_p)_{hnf}}\left(\frac{\partial^2 T}{\partial x^2} + \frac{\partial^2 T}{\partial y^2}\right) + \frac{1}{(\rho C_p)_{hnf}}\frac{16\sigma * T_h^3}{3k*}\left(\frac{\partial^2 T}{\partial x^2} + \frac{\partial^2 T}{\partial y^2}\right) + \frac{Q_0}{(\rho C_p)_{hnf}}(T - T_h) \tag{10}$$

2.1. Thermophysical Attributes of Hybrid Nanofluid

Here, ϕ_1 and ϕ_2 are the nanoparticle volume fractions, subscripts hnf and nf indicate hybrid and mono nanofluids, respectively, f indicates base fluid, and s_1 and s_2 specify nanomaterials.

$$\left.\begin{array}{l} \rho_{hnf} = (1-\phi_2)\left[(1-\phi_1)\rho_f + \phi_1\rho_{s_1}\right] + \phi_2\rho_{s_2}, \mu_{hnf} = \frac{\mu_f}{(1-\phi_1)^{2.5}(1-\phi_2)^{2.5}}, \\ \sigma_{hnf} = \frac{\sigma_{s_2}+2\sigma_{nf}-2\phi_2(\sigma_{nf}-\sigma_{s_2})}{\sigma_{s_2}+2\sigma_{nf}+\phi_2(\sigma_{nf}-\sigma_{s_2})} \times \sigma_{nf}, \sigma_{nf} = \frac{\sigma_{s_1}+2\sigma_f-2\phi_1(\sigma_f-\sigma_{s_1})}{\sigma_{s_1}+2\sigma_f+\phi_1(\sigma_f-\sigma_{s_1})} \times \sigma_f \\ k_{hnf} = \frac{k_{s_2}+2k_{nf}-2\phi_2(k_{nf}-k_{s_2})}{k_{s_2}+2k_{nf}+\phi_2(k_{nf}-k_{s_2})} \times k_{nf}, k_{nf} = \frac{k_{s_1}+2k_f-2\phi_1(k_f-k_{s_1})}{k_{s_1}+2k_f+\phi_1(k_f-k_{s_1})} \times k_f \\ (\rho C_p)_{hnf} = (1-\phi_2)\left[(1-\phi_1)(\rho C_p)_f + \phi_1(\rho C_p)_{s_1}\right] + \phi_2(\rho C_p)_{s_2} \end{array}\right\}$$

Table 1. Thermophysical properties of nanomaterials and base fluid (Reprinted with permission from Ref. [65]. Copyright 2022 Copyright Elsevier).

S. No.		Propylene Glycol—Water Mixture (f)	Paraffin Wax (s_1)	Sand (s_2)
1	$\rho(\mathrm{Kg/m^3})$	1020	900	2650
2	$C_p(\mathrm{J/Kg\ K})$	3342.75	2900	730
3	$k(\mathrm{W/m\ K})$	0.363	0.25	1.5

2.2. Similarity Transmutations

Similarity transmutations (Khan et al. [66]) in Equation (11) as:

$$\left.\begin{array}{l} \eta = \frac{y}{h(t)}, u = \frac{ax}{1-\gamma t}f', v = -\sqrt{\frac{av}{1-\gamma t}}f, \\ w = \frac{ax}{1-\gamma t}g, \theta = \frac{T-T_h}{T_w-T_h}, \Phi = \frac{C-C_h}{C_w-C_h} \end{array}\right\} \tag{11}$$

2.3. Transmuted Equations and Conditions

Transmutations satisfies Equation (1), and alters Equations (2)–(4), (6) and (10) as:

$$\frac{1}{H_1H_2}f''' - \frac{1}{2}S_q\eta f'' - S_q f' - f'^2 + ff'' - 2\Omega g + \frac{M}{H_1}f' = -\frac{(1-\gamma t)^2}{a^2 x}\frac{1}{\rho_f H_1}\frac{\partial p}{\partial x} \tag{12}$$

$$f'' - \frac{1}{2}S_q\eta f' - \frac{S_q}{2}f + ff' = -\frac{a}{(1-\gamma t)^2}\frac{1}{\rho_f H_1}\frac{\partial p}{\partial \eta} \tag{13}$$

$$\frac{1}{H_1H_2}g'' - \frac{1}{2}S_q\eta g' - S_q g + fg' - f'g + 2\Omega f' - \frac{M}{H_1}g = 0 \tag{14}$$

$$\left(\frac{R_a + H_3H_{31}}{H_4}\right)\frac{\theta''}{\mathrm{Pr}} + f\theta' - \frac{\eta}{2}S_q\theta' + \frac{N}{H_4}\theta = 0 \tag{15}$$

$$\frac{1}{Sc}\Phi'' + f\Phi' - \frac{S_q}{2}\eta\Phi' - \Gamma(1+\alpha_1\theta)^n Exp\left(-\frac{E_n}{1+\alpha_1\theta}\right)\Phi = 0 \tag{16}$$

and alters the conditions in Equation (7) as:

$$\left.\begin{array}{l} f(0) = S, f'(0) = 1, g(0) = 1, \theta(0) = 1, \Phi(0) = 1 \\ f(1) = \frac{S_q}{2}, f'(1) = 0, g(1) = 0, \theta(1) = 0, \Phi(1) = 0 \end{array}\right\} \tag{17}$$

where

$$\left.\begin{array}{l} H_1 = (1-\phi_1)^{2.5}(1-\phi_2)^{2.5}, H_2 = (1-\phi_2)\left[(1-\phi_1) + \phi_1\frac{\rho_{s_1}}{\rho_f}\right] + \phi_2\frac{\rho_{s_2}}{\rho_f}, H_{31} = \frac{k_{s_1}+2k_f-2\phi_1\left(k_f-k_{s_1}\right)}{k_{s_1}+2k_f+\phi_1\left(k_f-k_{s_1}\right)}, \\ H_3 = \frac{k_{s_2}+2H_{31}k_f-2\phi_2\left(H_{31}k_f-k_{s_2}\right)}{k_{s_2}+2H_{31}k_f+\phi_2\left(H_{31}k_f-k_{s_2}\right)}, H_4 = (1-\phi_2)\left[(1-\phi_1) + \phi_1\frac{(\rho C_p)_{s_1}}{(\rho C_p)_f}\right] + \phi_2\frac{(\rho C_p)_{s_2}}{(\rho C_p)_f} \end{array}\right\}.$$

and

$$\left.\begin{array}{l} S_q = \frac{d}{a}, \Omega = \frac{\omega}{a}, M = \frac{\sigma B_0^2}{\rho_f a}, \mathrm{Pr} = \frac{\mu(C_p)_f}{k_f}, R_a = \frac{16}{3}\frac{\sigma * T_h^3}{k_f k*}, \\ N = \frac{Q_0(1-dt)}{a\left(\rho C_p\right)_f}, \Gamma = \frac{k_r(1-dt)}{a}, \alpha_1 = \frac{T_w-T_h}{T_h}, E_n = \frac{E_a}{k_1 T_h}, S = \frac{V_0}{ah} \end{array}\right\}$$

Applied cross-differentiation on Equations (12) and (13) leads to a simplified fourth-order differential, where the similarity solution is maintained, the number of the independent variables is reduced, and the pressure term from Equations (2) and (3) is disregarded. The consequential equation is:

$$\frac{1}{H_1H_2}f^{iv} - \frac{S_q}{2}(\eta f''' + 3f'') - f'f'' + ff''' - 2\Omega g' - \frac{M}{H_1}f'' = 0 \tag{18}$$

2.4. Physical Parameters

Near the lower plate, surface drag force is defined as (Alzahrani et al. [17]):

$$C_{f_0} = \frac{\mu_{hnf}\left(\frac{\partial v}{\partial x} + \frac{\partial u}{\partial y}\right)\Big|_{y=0}}{\rho_{hnf}u_w^2}, C_{g_0} = \frac{\mu_{hnf}\left(\frac{\partial w}{\partial y}\right)\Big|_{y=0}}{\rho_{hnf}u_w^2} \tag{19}$$

Near the upper plate, the same (surface drag force) is defined as:

$$C_{f_1} = \frac{\mu_{hnf}\left(\frac{\partial v}{\partial x} + \frac{\partial u}{\partial y}\right)\Big|_{y=h(t)}}{\rho_{hnf}u_w^2}, C_{g_1} = \frac{\mu_{hnf}\left(\frac{\partial w}{\partial y}\right)\Big|_{y=h(t)}}{\rho_{hnf}u_w^2} \tag{20}$$

With the aid of Equations (11), (19) and (20), it can be rewritten in dimensionless form as:

$$C_{f_0} = \frac{1}{H_1H_2}\frac{1}{\sqrt{\mathrm{Re}_x}}f''(0), C_{g_0} = \frac{1}{H_1H_2}\frac{1}{\sqrt{\mathrm{Re}_x}}g'(0) \tag{21}$$

and

$$C_{f_1} = \frac{1}{H_1H_2}\frac{1}{\sqrt{\mathrm{Re}_x}}f''(1), C_{g_1} = \frac{1}{H_1H_2}\frac{1}{\sqrt{\mathrm{Re}_x}}g'(1) \tag{22}$$

where $\mathrm{Re}_x = \frac{xu_w}{v_f}$ (local Reynolds number).

Formulae to find transfer rates (heat and mass) (or Nusselt and Sherwood numbers) near lower and upper plates are:

$$Nu_0 = \frac{x\,q_w|_{y=0}}{k_f(T_w - T_h)}, Nu_1 = \frac{x\,q_w|_{y=h(t)}}{k_f(T_w - T_h)} \text{ and } Sh_0 = \frac{x\,s_w|_{y=0}}{D_m(C_w - C_h)}, Sh_1 = \frac{x s_w|_{y=h(t)}}{D_m(C_w - C_h)} \tag{23}$$

where the wall heat flux, $q_w = -\left(K_{hnf} + \frac{16\sigma * T_h^3}{3k*}\right)\frac{\partial T}{\partial y}$ and the wall mass flux,

$$s_w = -D_m \frac{\partial C}{\partial y} \tag{24}$$

With the aid of Equations (8) and (24), formulae in (23) can be rewritten as:

$$Nu_0 = -\left(\frac{k_{hnf}}{k_f} + R_a\right)\theta'(0), Nu_1 = -\left(\frac{k_{hnf}}{k_f} + R_a\right)\theta'(1)$$

and

$$Sh_0 = -\Phi'(0), Sh_1 = -\Phi'(1)$$

2.5. Entropy Generation and Bejan Number

The volumetric rate of entropy generation (dimensional form) for the hybrid nanofluid flow among two parallel plates is specified as:

$$\begin{aligned} S_{gen} = {} & \frac{k_{hnf}}{T_h^2}\left[\left(\frac{\partial T}{\partial x}\right)^2 + \left(\frac{\partial T}{\partial y}\right)^2\right] + \frac{1}{T_h^2}\frac{16}{3}\frac{\sigma * T_\infty^3}{k*}\left[\left(\frac{\partial T}{\partial x}\right)^2 + \left(\frac{\partial T}{\partial y}\right)^2\right] + \frac{\mu_{hnf}}{T_h}\varphi + \frac{\sigma(B(t))^2}{T_2}\left(u^2 + w^2\right) \\ & + \frac{\overline{R}D_m}{C_h}\left[\left(\frac{\partial C}{\partial x}\right)^2 + \left(\frac{\partial C}{\partial y}\right)^2\right] + \frac{\overline{R}D_m}{T_h}\left(\frac{\partial C}{\partial x}\frac{\partial T}{\partial x} + \frac{\partial C}{\partial y}\frac{\partial T}{\partial y}\right) \end{aligned} \tag{25}$$

where

$$\varphi = 4\left(\frac{\partial u}{\partial x}\right)^2 + \left(\frac{\partial v}{\partial x} + \frac{\partial u}{\partial y}\right)^2 + \left(\frac{\partial w}{\partial x}\right)^2 + \left(\frac{\partial w}{\partial y}\right)^2 \tag{26}$$

and $\overline{R}$ is the universal gas constant.

The non-dimensional form of Equation (25) is:

$$\begin{aligned} N_{EG} = {} & (H_3H_{31} + R_a)\alpha_1\theta'^2 + Br\left(4f'^2 + g^2\right) + Br_1\left(f''^2 + g'^2\right) + \frac{BrM}{H_2}\left(f'^2 + g^2\right) \\ & + H * \frac{\alpha_2}{\alpha_1}\Phi'^2 + H * \Phi'\theta' \end{aligned} \tag{27}$$

Entropy generation N_{EG}, Brinkman number Br, local Brinkman number Br_1, diffusion parameter $H*$, and the concentration ratio parameter α_2 are specified as:

$$\left.\begin{aligned} & N_{EG} = \frac{v(1-dt)T_h S_G}{a(T_w - T_h)k_f}, Br = \frac{\mu v^2}{h^2(T_w - T_h)k_f}, Br_1 = \frac{\mu u_w^2}{(T_w - T_h)k_f}, \\ & H* = \frac{\overline{R}D_m(C_w - C_h)}{k_f}, \alpha_2 = \frac{C_w - C_h}{C_h} \end{aligned}\right\}$$

By using the below formula, we can evaluate the Bejan number:

$$Be = \frac{\text{Entropy generation on account of heat and mass transfer}}{\text{Total entropy generation}}$$

By using Equation (27), Be can be articulated as

$$Be = \frac{(H_3H_{31} + R_a)\alpha_1\theta'^2 + H * \frac{\alpha_2}{\alpha_1}\Phi'^2 + H * \Phi'\theta'}{(H_3H_{31} + R_a)\alpha_1\theta'^2 + Br\left(4f'^2 + g^2\right) + Br_1\left(f''^2 + g'^2\right) + \frac{BrM}{H_2}\left(f'^2 + g^2\right) + H * \frac{\alpha_2}{\alpha_1}\Phi'^2 + H * \Phi'\theta'}.$$

3. Numerical Procedure

The fourth-order Runge–Kutta method and shooting procedure combination are engaged to solve Equations (14)–(16) and (18), with the conditions presented in Equation (17).

Let

$$x_1 = f, x_2 = f', x_3 = f'', x_4 = f''', x_5 = g, x_6 = g', x_7 = \theta, x_8 = \theta', x_9 = \Phi, x_{10} = \Phi'$$

Then, using Equations (11)–(13) and (15), we can develop the subsequent system of ODEs of the first-order:

$$\left.\begin{array}{l} x_1{}' = x_2, \\ x_2{}' = x_3, \\ x_3{}' = x_4, \\ x_4{}' = H_1H_2\left[\frac{S_q}{2}(\eta x_4 + 3x_3) + x_2x_3 - x_1x_4 + 2\Omega x_6 + \frac{M}{H_1}x_3\right], \\ x_5{}' = x_6, \\ x_6{}' = H_1H_2\left[\frac{S_q}{2}\eta x_6 + S_q x_5 + x_2x_5 - x_1x_6 - 2\Omega x_2 + \frac{M}{H_1}x_5\right], \\ x_7{}' = x_8 \\ x_8{}' = -\mathrm{Pr}\left(\frac{H_4}{R_a + H_3H_{31}}\right)\left[x_1x_8 - \frac{\eta}{2}S_q x_8 + \frac{1}{H_2H_4}\left[E_c\left(4x_2^2 + x_6^2\right) + E_{cx}\left(x_3^2 + x_6^2\right)\right] + Nx_7\right] \\ x_9{}' = x_{10} \\ x_{10}{}' = -Sc\left[x_1x_{10} - \frac{S_q}{2}\eta x_{10} - \Gamma(1 + \alpha_1x_7)^n Exp\left(-\frac{E_n}{1+\alpha_1x_7}\right)x_9\right] \end{array}\right\} \quad (28)$$

with the initial conditions:

$$\left.\begin{array}{l} x_1(0) = S, x_2(0) = 1, x_3(0) = \varsigma_1, x_4(0) = \varsigma_2, x_5(0) = 1 \\ x_6(0) = \varsigma_3, x_7(0) = 1, x_8(0) = \varsigma_4, x_9(0) = 1, x_{10}(0) = \varsigma_5 \end{array}\right\} \quad (29)$$

Here $\varsigma_1, \varsigma_2, \varsigma_3, \varsigma_4$, and ς_5 are the required introductory guesses to sort out the solution. The fourth-order R–K scheme is imposed to obtain the solution. Afterward, we calculate $x_1(1), x_2(1), x_5(1), x_7(1), x_9(1)$ values, and compare them with the current values of the equivalent. If they are not appropriately equivalent, using the shooting strategy to change the estimations $x_3(0), x_4(0), x_6(0), x_8(0), x_{10}(0)$ obtains a decent solution. This procedure will be repeated until we achieve the desired precision.

4. Validation

We verified our outcomes with the earlier results for friction factor (with two methods) under special circumstances, such as $\phi_1 = \phi_2 = 0$ and $M = 0.5$, and detected an acceptable agreement (see Table 2).

Table 2. Verification of present results with earlier outcomes under special conditions.

		Munawar et al. [3]		**Current Study**			
				Shooting Method		**Bvp4c Method**	
S	S_q	$f''(1)$	$g'(1)$	$f''(1)$	$g'(1)$	$f''(1)$	$g'(1)$
0	2	−4.5827056	−1.2304429	−4.582984	−1.230411	−4.582984	−1.230411
0.3		−2.6227888	−0.8059641	−2.622739	−0.805942	−2.622739	−0.805942
0.6		−0.7312990	−0.3611836	−0.731299	−0.361177	−0.731299	−0.361177
0.9		1.0924124	0.1059088	1.092497	0.105892	1.092497	0.105892
1.2		2.8491655	0.5975976	2.849166	0.597586	2.849166	0.597586
0.5	−1	7.7031724	3.0250739	7.703171	3.025059	7.703171	3.025059
	0	4.8235909	1.4031897	4.823590	1.403201	4.823590	1.403201
	1	1.8091719	0.2966841	1.809170	0.296684	1.809170	0.296684
	2	−1.3542292	−0.5118183	−1.354199	−0.511811	−1.354199	−0.511811
	3	−4.6700503	−1.1328529	−4.670051	−1.132848	−4.670051	−1.132848

5. Discussion

The impacts of pertinent parameters on the flow are explained in two situations. The first situation dealt with the comparison of two cases, i.e., hybrid and mono nanofluids, and the second situation dealt with the comparison of two cases, i.e., positive squeezing parameter (upper plate proceeds in the direction of the lower plate) and negative squeezing parameter (upper plate is moving apart from the lower plate).

5.1. Velocity Profiles

Fluid particles try to change their direction within the sight of the magnetic field. So, the velocity of the fluid deprecates with a larger magnetic field (Figures 2–4). Figures 5–7 account for the impact of the squeezing number S_q on the velocity profiles. Generally, with the elevation in squeezing number, there is an increment in the pressure of the fluid. As a result, intensification in fluid velocity occurs. It is evident from Figure 8 that the volumetric nanoparticle parameter alleviates the normal velocity in x-direction because of the enhancement in fluid viscosity. Since the particles move from the lower plate to the upper plate, initially, the concentration of particles is higher at the lower plate than at the upper plate. So, the larger rotation parameter deprecates normal velocity (in x-direction) in the lower half, and ameliorates the same in the upper half (Figure 9).

5.2. Temperature Profiles

Figures 10 and 11 exhibit the impression of the heat source parameter N on the temperature profile. It is seen that it escalates temperature. Typically, a larger heat source parameter causes the proliferation of additional heat within the fluid and, in turn, enhances the thickness of the thermal boundary layer. The radiation parameter mitigates fluid temperature (Figures 12 and 13). From these outcomes, it is interesting to remark that the mono nanofluid profile is high in contrast with the hybrid nanofluid profile in the second situation, and the complete opposite behavior observed in the first situation. Larger volumetric nanoparticle parameters generate more friction among particles, which leads to the escalation in fluid temperature (Figure 14).

5.3. Concentration Profiles

Mass diffusivity minifies with a larger Schmidt number. So, concentration minifies with a larger Schmidt number (Figures 15 and 16). Figures 17 and 18 elucidate the impression of activation energy on the concentration profile. Generally, an increase in activation energy leads to a reduction in the threshold energy of the fluid, which, in turn, demonstrates the average kinetic energy. From the above condition, we can conclude that the average kinetic energy is less. Hence, diffusion will be less, which leads to a high concentration of the fluid. It is perceived that the fluid concentration is minified with a larger reaction rate parameter (Figures 19 and 20). Higher temperature difference leads to lower molecular diffusivity. So, fluid concentration is minified with higher α_1 (Figures 21 and 22). We observe that profiles look higher in the case of a positive squeezing number contrasted with a negative squeezing number.

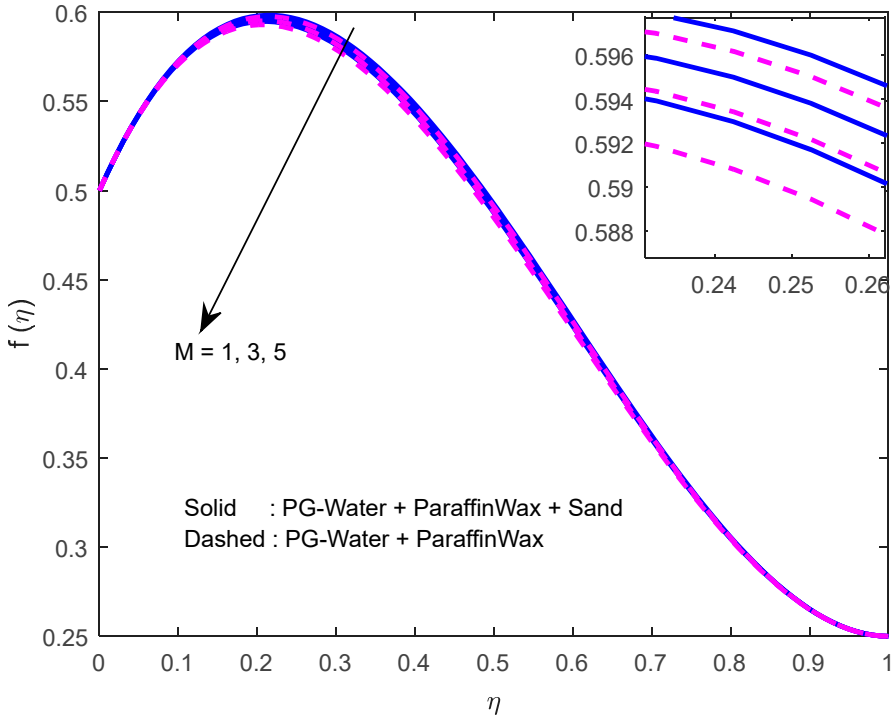

Figure 2. Effect of the magnetic field parameter on the velocity profile in y-direction.

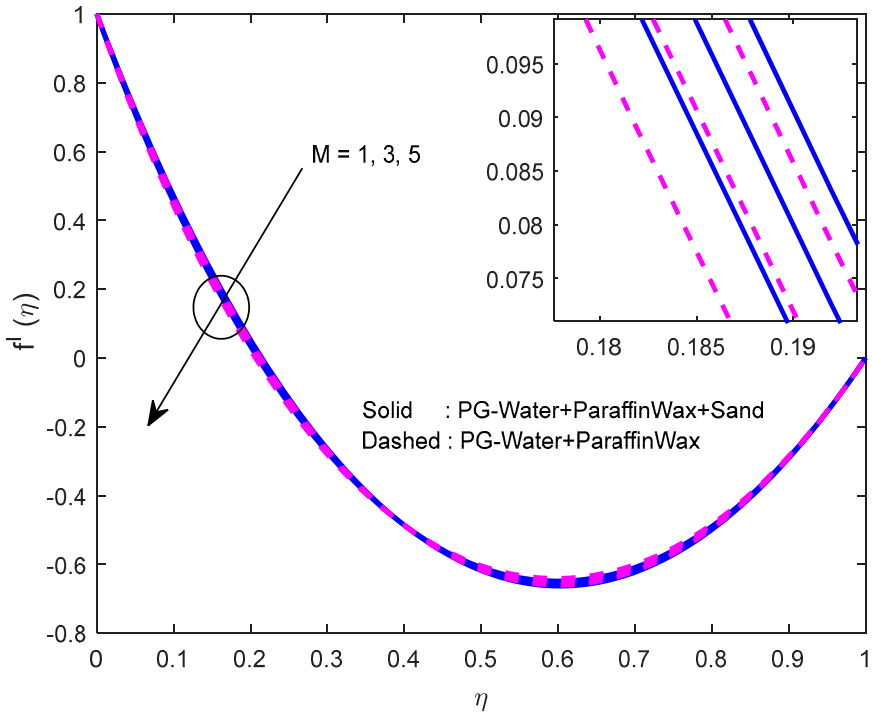

Figure 3. Effect of the magnetic field parameter on the velocity profile in x-direction.

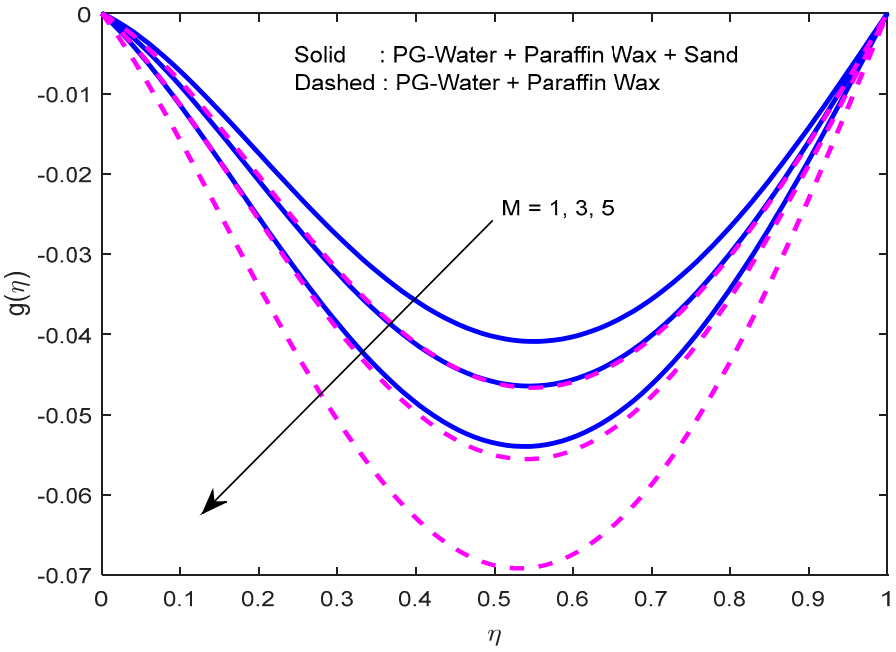

Figure 4. Effect of the magnetic field parameter on velocity profile in z-direction.

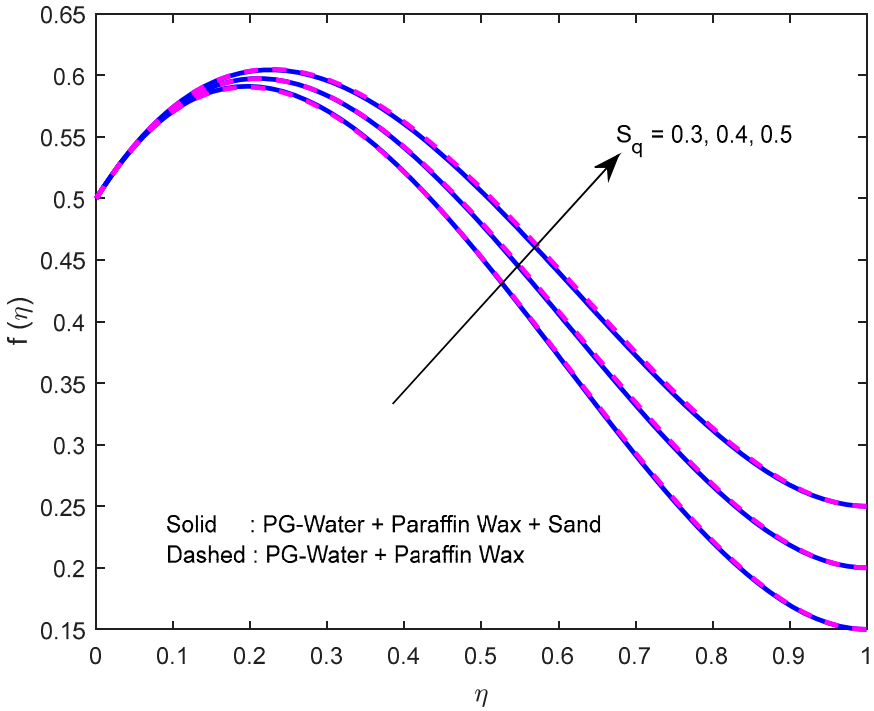

Figure 5. Effect of the squeeze number on velocity profile in y-direction.

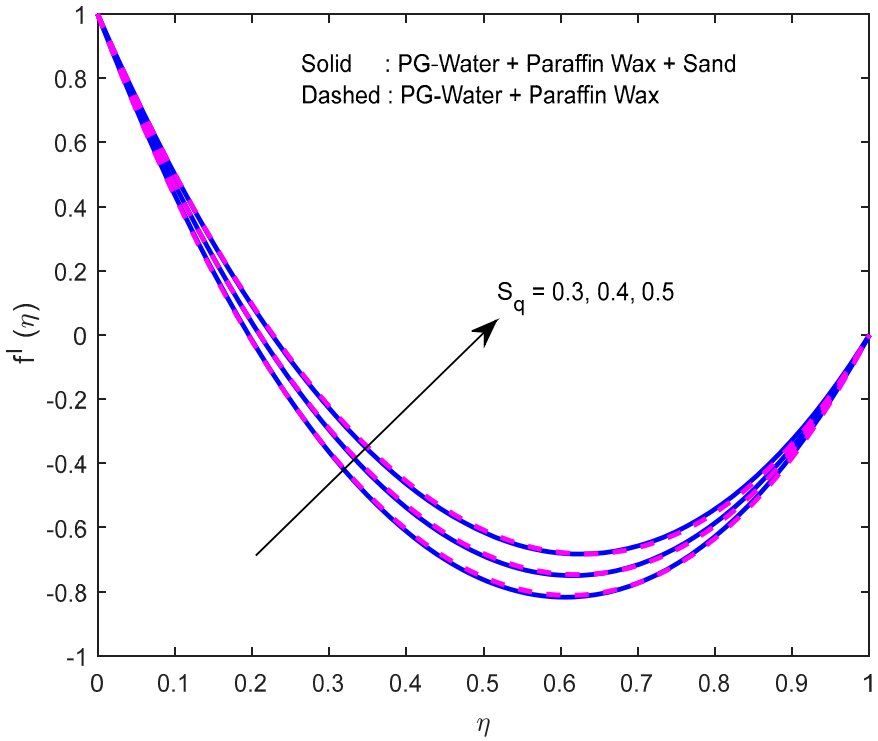

Figure 6. Effect of the squeeze number on the velocity profile in x -direction.

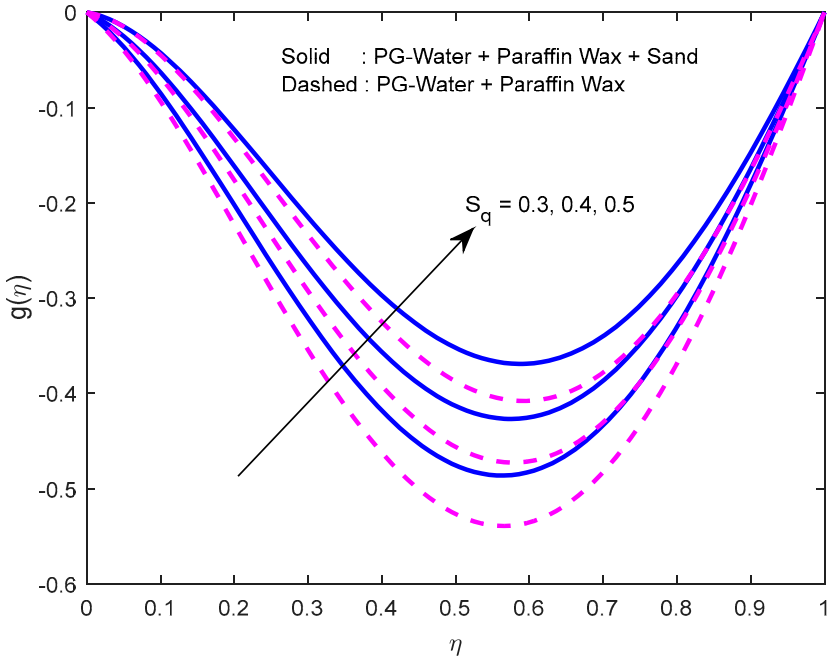

Figure 7. Effect of the squeeze number on the velocity profile in z-direction.

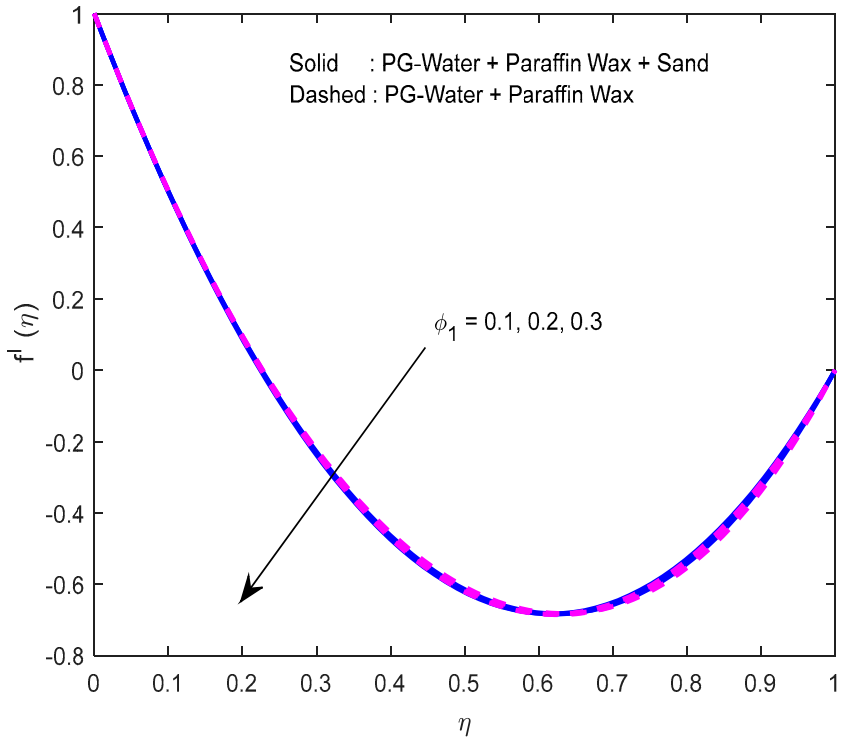

Figure 8. Effect of the nanoparticle volume fraction parameter on the velocity profile in x-direction.

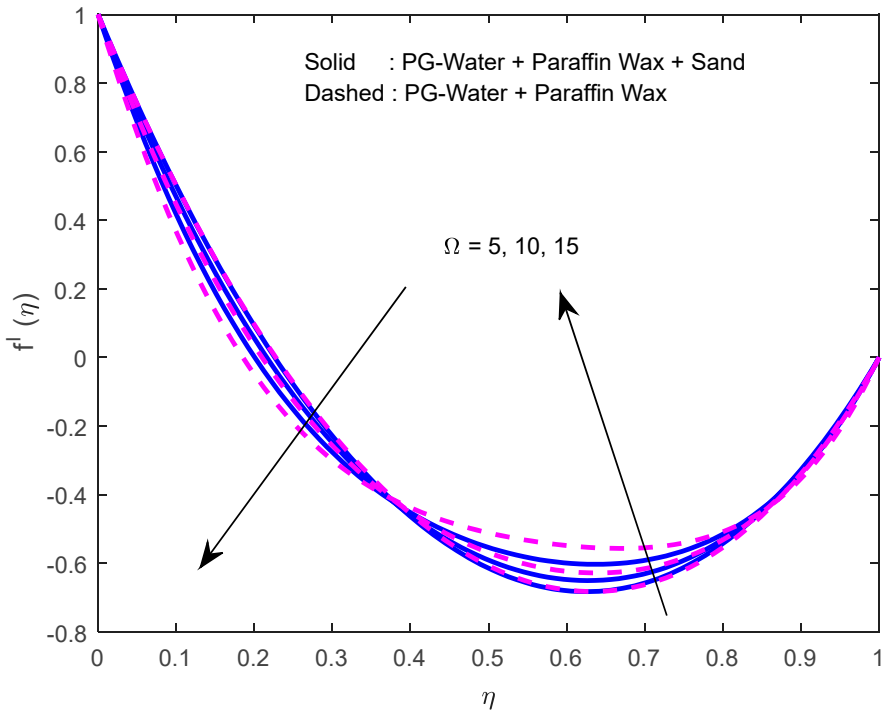

Figure 9. Effect of the rotation parameter on the velocity profile in x-direction.

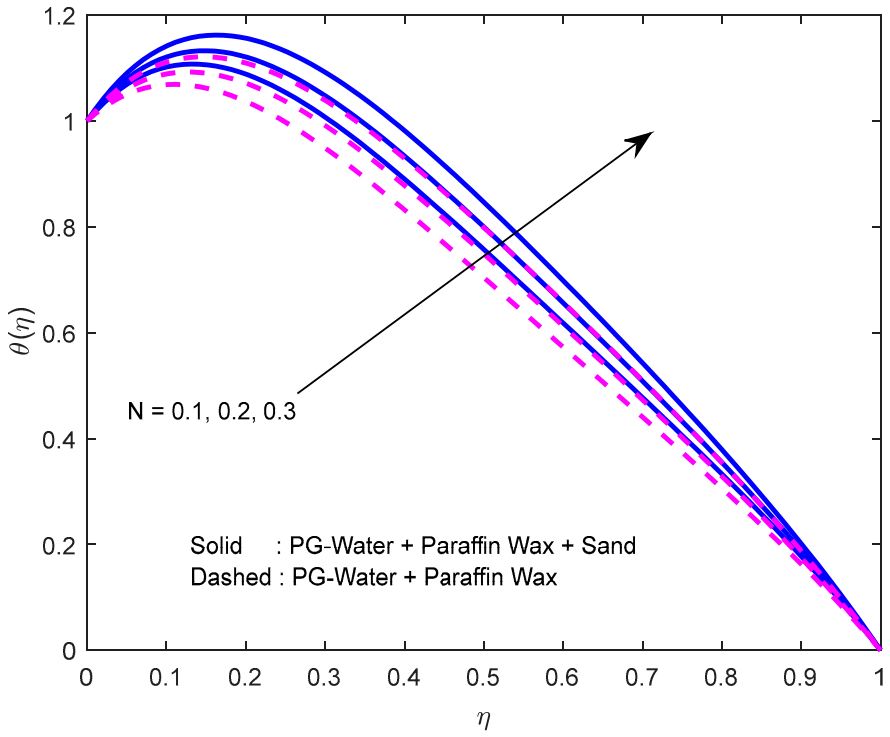

Figure 10. Effect of the heat source parameter on the temperature profile.

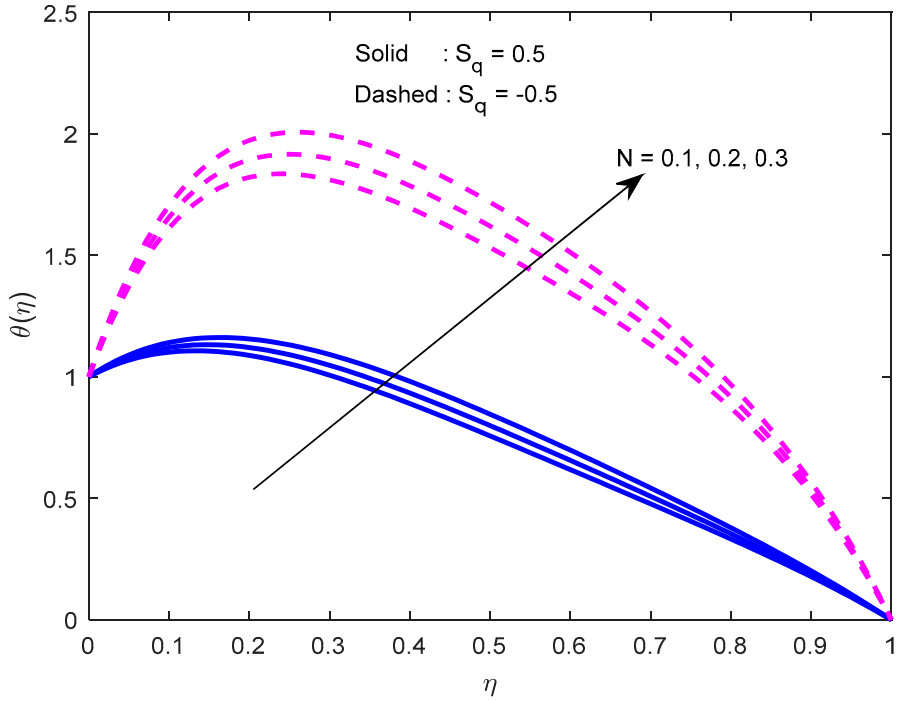

Figure 11. Effect of the heat source parameter on the temperature profile, with varying squeeze numbers.

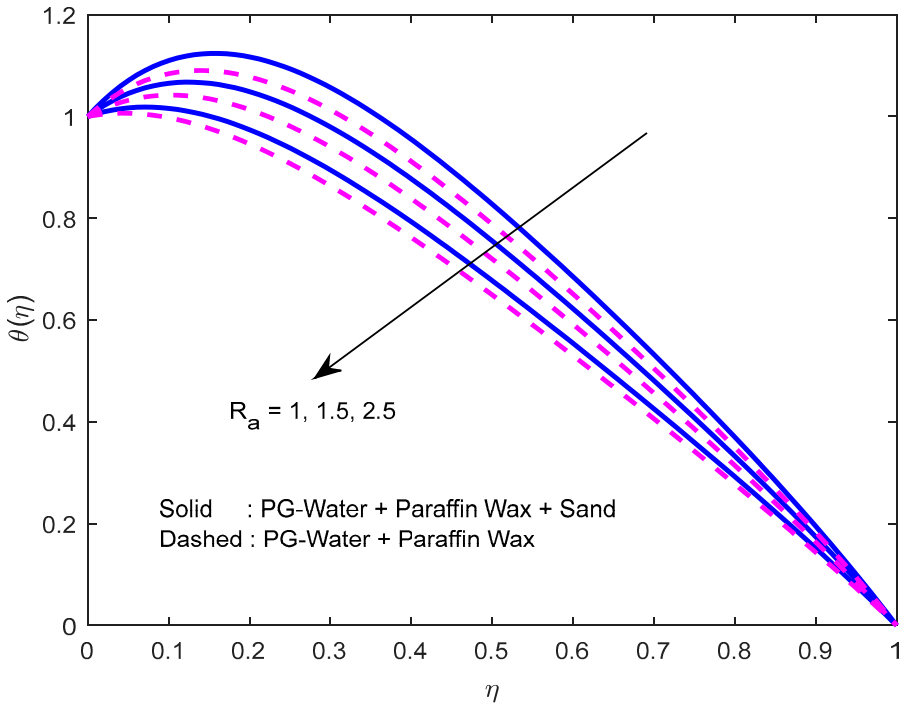

Figure 12. Effect of radiation parameter on the temperature profile.

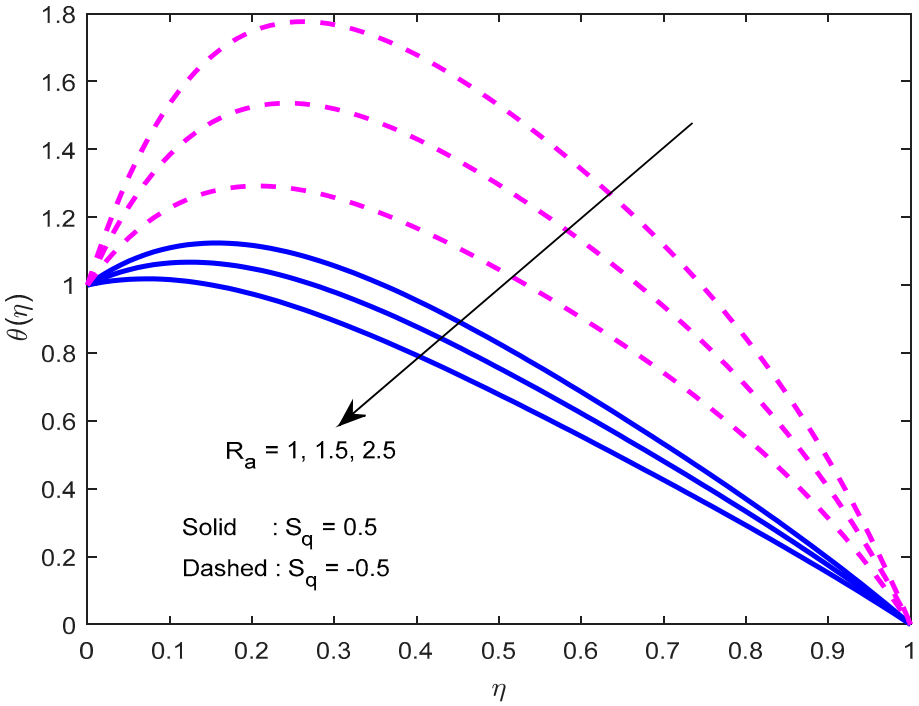

Figure 13. Effect of the radiation parameter on the temperature profile, with varying squeezing numbers.

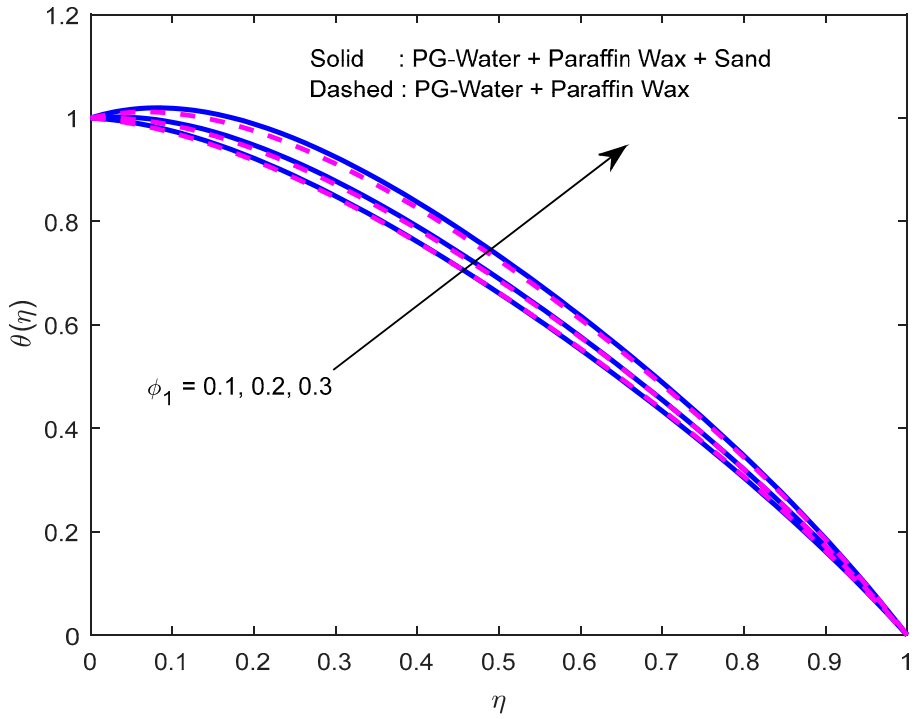

Figure 14. Effect of the nanoparticle volume fraction parameter on the temperature profile.

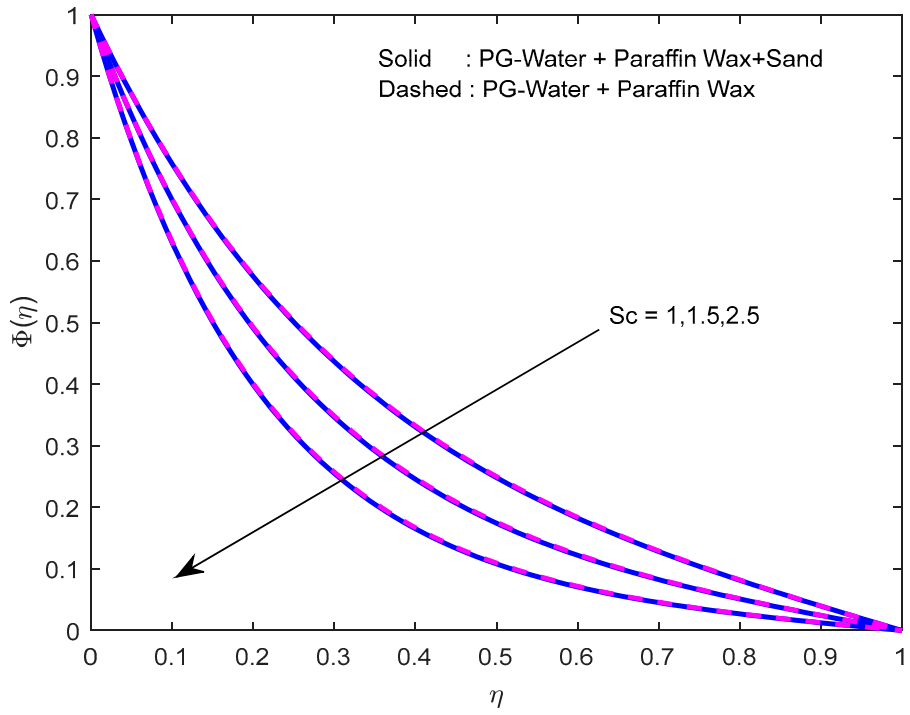

Figure 15. Effect of the Schmidt number on the concentration profile for various nanofluids.

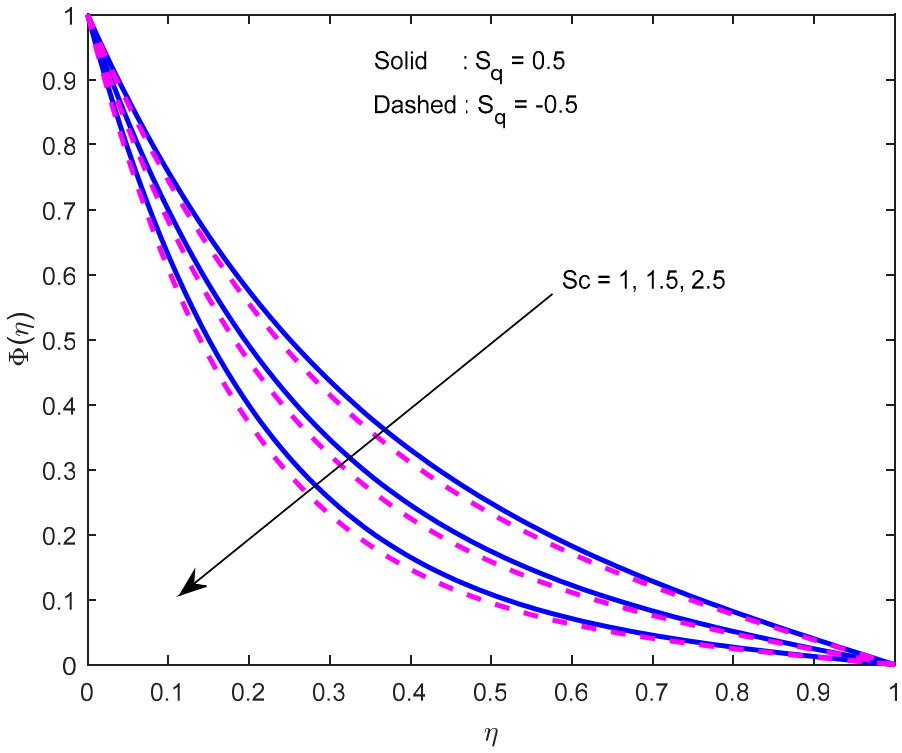

Figure 16. Effect of the Schmidt number on the concentration profile for various squeeze numbers.

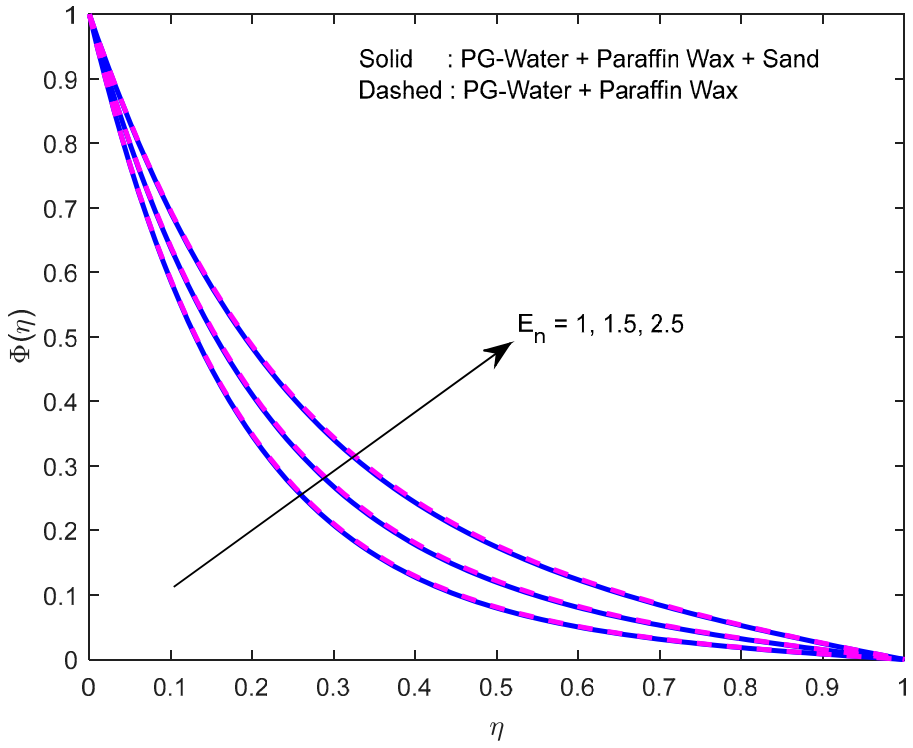

Figure 17. Effect of the activation energy parameter on the concentration profile.

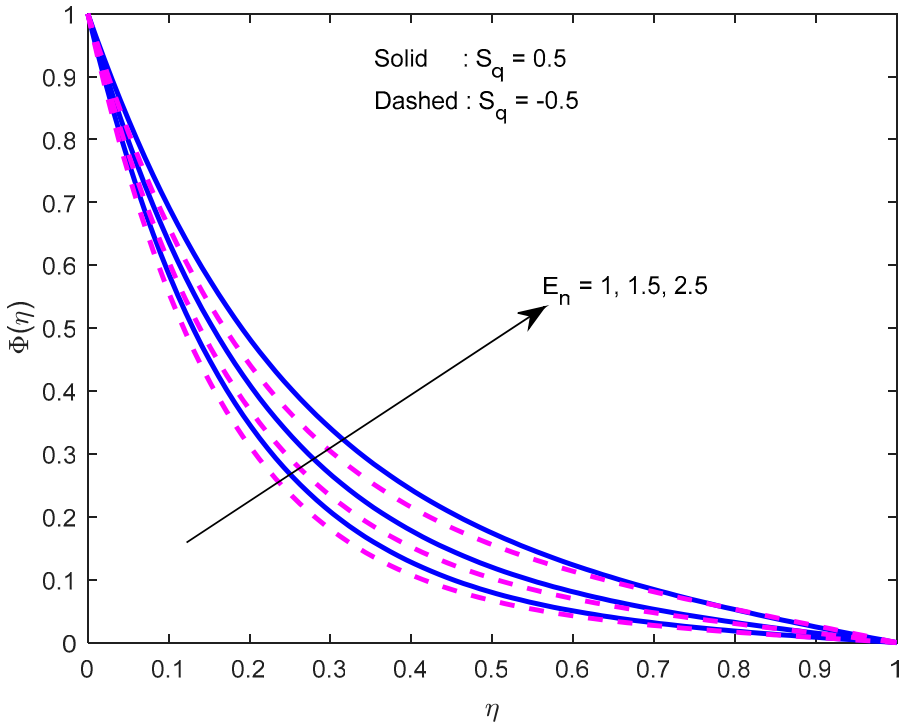

Figure 18. Effect of the activation energy parameter on the concentration profile for various squeeze numbers.

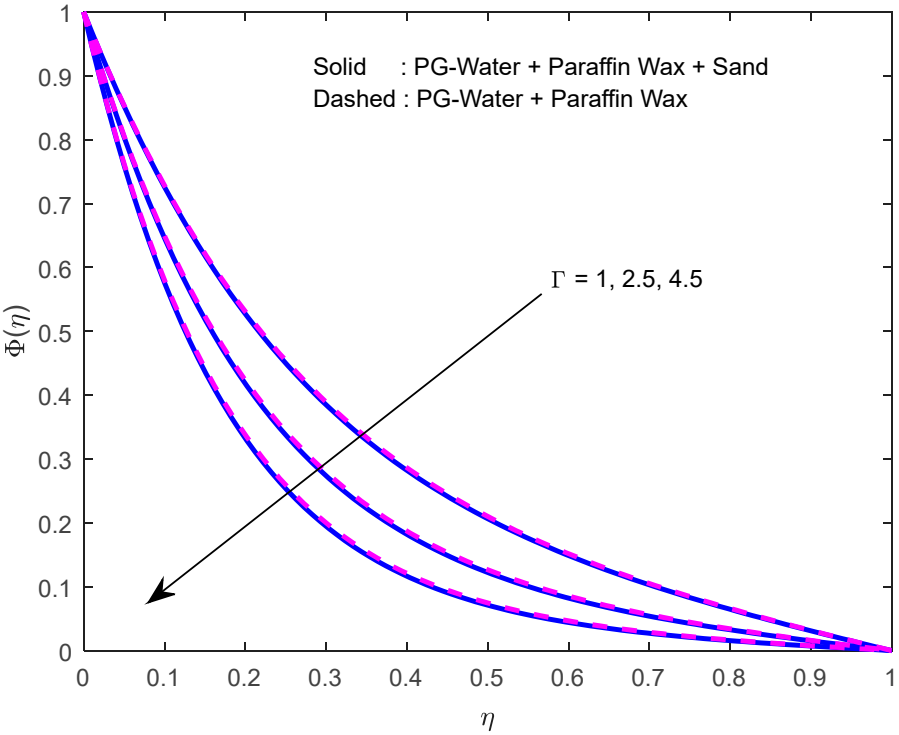

Figure 19. Effect of the reaction rate parameter on the concentration profile.

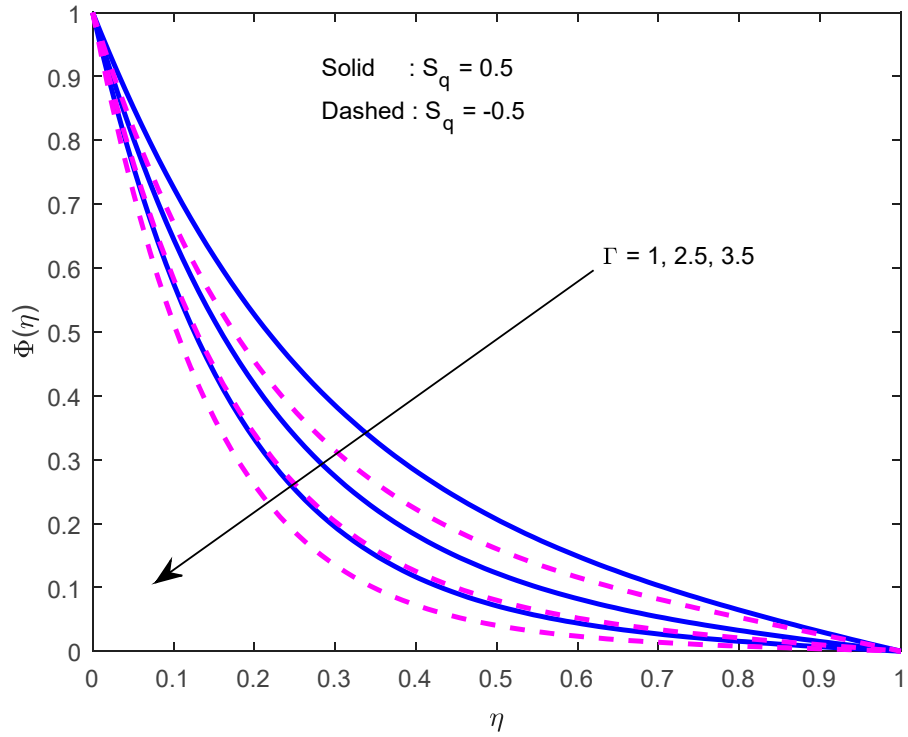

Figure 20. Effect of the reaction rate parameter on the concentration profile for various squeeze numbers.

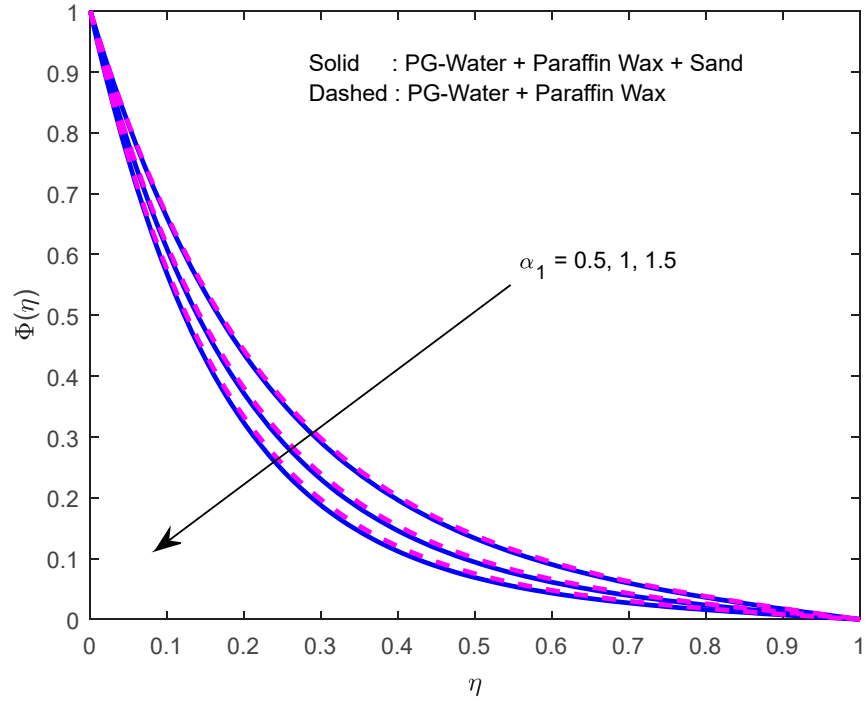

Figure 21. Effect of the temperature difference parameter on the concentration profile.

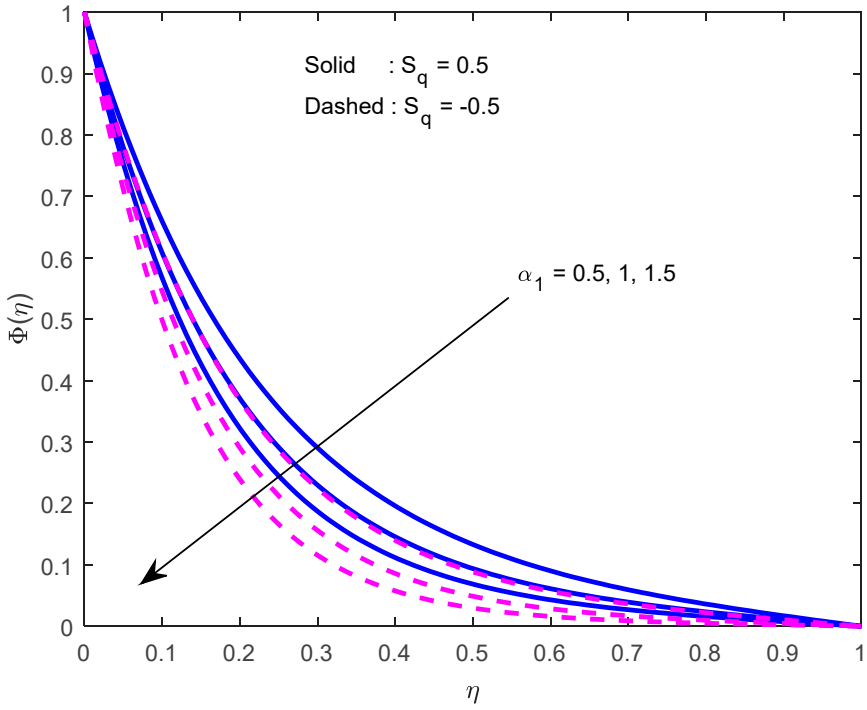

Figure 22. Effect of the temperature difference parameter on the concentration profile for various squeeze numbers.

5.4. Statistical Analysis of Physical Parameters Using Correlation Coefficient

The correlation coefficient is a numerical measure of the association between two factors. The value of the coefficient lies between -1 (negative association) and 1 (positive association).

One can evaluate the correlation coefficient using:

$$\gamma = \frac{r(\sum yz) - (\sum y)(z)}{\sqrt{\left[r\sum y^2 - (\sum y)^2\right]\left[r\sum z^2 - (\sum z)^2\right]}}$$

Probable error (P.E) of the correlation coefficient helps with choosing the exactness and reliability of the coefficient value. The importance of the correlation relies upon the association between the coefficient value (γ) and P.E. If $\frac{|\gamma|}{P.E} > 6$ (or $|\gamma| > 6P.E$), then the correlation is significant, and if $|\gamma| < P.E$, then we say that the correlation is insignificant.

One can evaluate P.E by using $P.E = 0.6745\frac{1-\gamma^2}{\sqrt{r}}$ where r is the number of observations.

We conducted a statistical analysis through a correlation coefficient to understand the impression of some important parameters on surface friction factor and transfer rates of heat and mass. Tables 3 and 4 elucidate the relationship between surface drag force and some parameters (squeezing number, magnetic field, rotating parameter, and nanoparticle volume fraction parameter) near the lower and upper plates in two instances i.e., hybrid and mono nanofluids. It is witnessed that, except for the squeezing number, the other parameters (magnetic field, rotation parameter, and nanoparticle volumetric parameter) have a strong negative relationship with the friction factor at the lower plate. That means those three parameters deprecate the shear stress near the lower plate. Near the upper plate, it is acknowledged that the aforementioned parameters, except magnetic field, show reverse behavior on friction factor. Tables 5 and 6 exhibit the relationship among N,R_a, and the Nusselt number near the lower and upper plates. We find a strong negative relationship between N and Nusselt number, and a strong positive relationship between R_a and the heat transfer rate near the lower plate. This means that near the lower plate and larger heat source deprecates the heat transfer rate, and radiation parameter escalates the same. Near the upper plate, except for the radiation parameter, the heat source parameter

displays a strong positive relationship with the heat transfer rate. Tables 7 and 8 elucidate the relationship between $Sc, E_n, \Gamma, \alpha_1$, and the mass transfer rate near both plates. It is identified that the Sherwood number has a strong positive relationship with Sc, Γ, α_1, and a strong negative relationship with E_n, near the lower plate. This means that the Sherwood number minifies with larger Sc, Γ, α_1, and intensifies with larger E_n. It is noticed that the complete opposite relationship between $Sc, E_n, \Gamma, \alpha_1$ and the mass transfer rate occurs near the upper plate.

Table 3. Correlation coefficient (γ) and probable error $(P.E)$ for surface drag force at the lower plate.

	C_{f_0}					
	Hybrid Nanofluid			**Nanofluid**		
	γ	$P.E$	$\frac{\lvert\gamma\rvert}{P.E}$	γ	$P.E$	$\frac{\lvert\gamma\rvert}{P.E}$
M	−0.9999	0.000044	22725	−0.9999	0.000044	22725
S_q	0.9870	0.005630	175.31	0.9792	0.008990	108.92
Ω	−0.9661	0.014555	66.38	−0.9666	0.014337	67.42
ϕ_1	−0.9296	0.029634	31.37	−0.9281	0.030245	30.69

Table 4. Correlation coefficient (γ) and probable error $(P.E)$ for surface drag force at the upper plate.

	C_{f_1}					
	Hybrid Nanofluid			**Nanofluid**		
	γ	$P.E$	$\frac{\lvert\gamma\rvert}{P.E}$	γ	$P.E$	$\frac{\lvert\gamma\rvert}{P.E}$
M	−0.9953	0.002051	485.28	−0.9725	0.011828	82.22
S_q	−0.9999	0.000044	22725	−0.9999	0.000044	22725
Ω	0.9655	0.014795	65.26	0.9655	0.014795	65.26
ϕ_1	0.9316	0.028827	32.32	0.9316	0.028827	32.32

Table 5. Correlation coefficient (γ) and probable error $(P.E)$ for local Nusselt number at the lower plate.

	Nu_0					
	Hybrid Nanofluid			**Nanofluid**		
	γ	$P.E$	$\frac{\lvert\gamma\rvert}{P.E}$	γ	$P.E$	$\frac{\lvert\gamma\rvert}{P.E}$
N	−0.9999	0.000044	22725	−0.9999	0.000044	22725
R_a	0.9999	0.000044	22725	0.9999	0.000044	22725

Table 6. Correlation coefficient (γ) and probable error $(P.E)$ for local Nusselt number at the upper plate.

	Nu_1					
	Hybrid Nanofluid			**Nanofluid**		
	γ	$P.E$	$\frac{\lvert\gamma\rvert}{P.E}$	γ	$P.E$	$\frac{\lvert\gamma\rvert}{P.E}$
N	0.9996	0.000174	5744.83	0.9996	0.000174	5744.83
R_a	0.9999	0.000044	22725	0.9999	0.000044	22725

Table 7. Correlation coefficient (γ) and probable error $(P.E)$ for local Sherwood number at the lower plate.

	Sh_0					
	Hybrid Nanofluid			**Nanofluid**		
	γ	$P.E$	$\frac{\lvert\gamma\rvert}{P.E}$	γ	$P.E$	$\frac{\lvert\gamma\rvert}{P.E}$
Sc	0.9997	0.000130	7690	0.9997	0.000130	7690
E_n	−0.9832	0.007267	135.3	−0.9831	0.007310	134.49
Γ	0.9999	0.000044	22725	0.9999	0.000044	22725
α_1	0.9989	0.000480	2081.04	0.9989	0.000480	2081.04

Table 8. Correlation coefficient (γ) and probable error $(P.E)$ for local Sherwood number at the upper plate.

	Sh_1					
	Hybrid Nanofluid			**Nanofluid**		
	γ	$P.E$	$\frac{\lvert\gamma\rvert}{P.E}$	γ	$P.E$	$\frac{\lvert\gamma\rvert}{P.E}$
Sc	−0.9824	0.007616	128.99	−0.9839	0.006983	140.9
E_n	0.9954	0.002007	495.96	0.9947	0.002313	430.05
Γ	−0.9999	0.000044	22725	−0.9999	0.000044	22725
α_1	−0.9975	0.001091	914.3	−0.9981	0.000829	1203.98

5.5. Entropy Generation and Bejan Number Profiles

Since there is a direct relationship between entropy generation and the temperature of the fluid, we can deduce that M, Br are useful in enhancing entropy generation (Figures 23 and 24). Figure 25 explicates the fact that the squeezing number minimizes entropy generation. We observe from Figures 26 and 27 that the Bejan number minifies with larger M, Br (because, in each case, the irreversibility of the heat and mass transfer is eclipsed by the unchangeability of the other terms, including fluid friction). Figure 28 reveals that the squeezing number escalates the Bejan number.

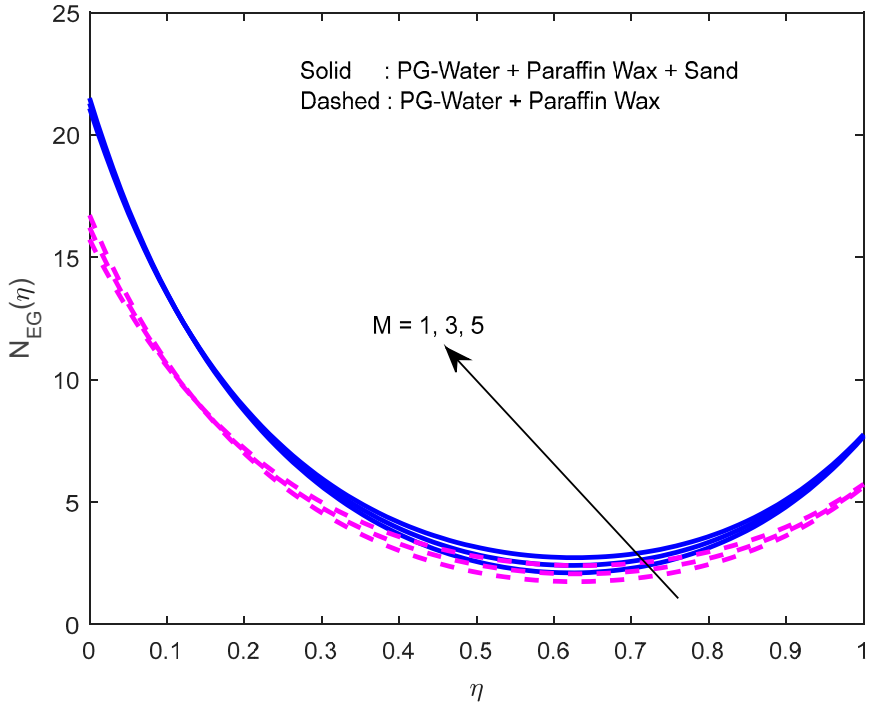

Figure 23. Effect of the magnetic field parameter on the entropy generation profile.

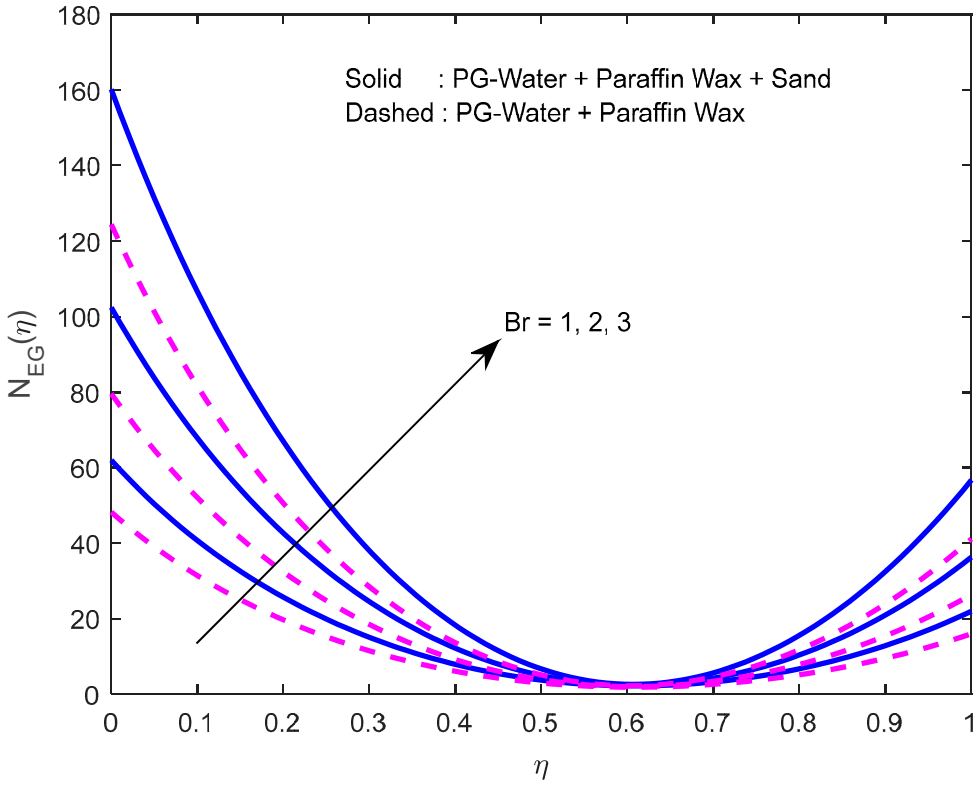

Figure 24. Effect of the Brinkmann number on the entropy generation profile.

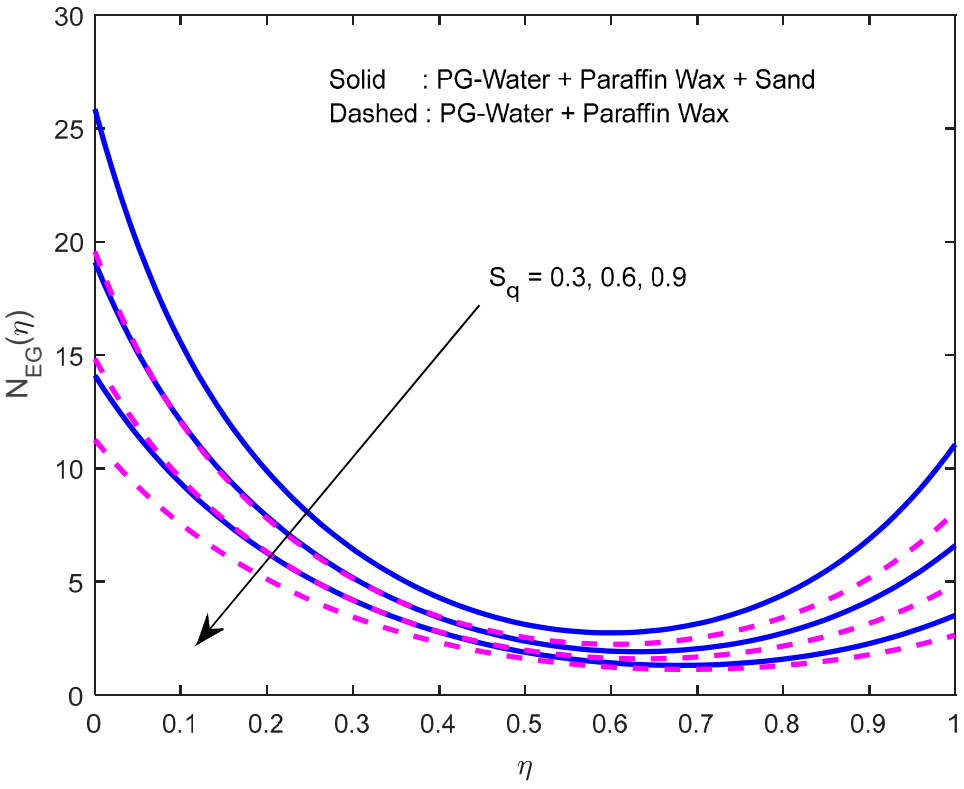

Figure 25. Effect of the squeeze number on the entropy generation profile.

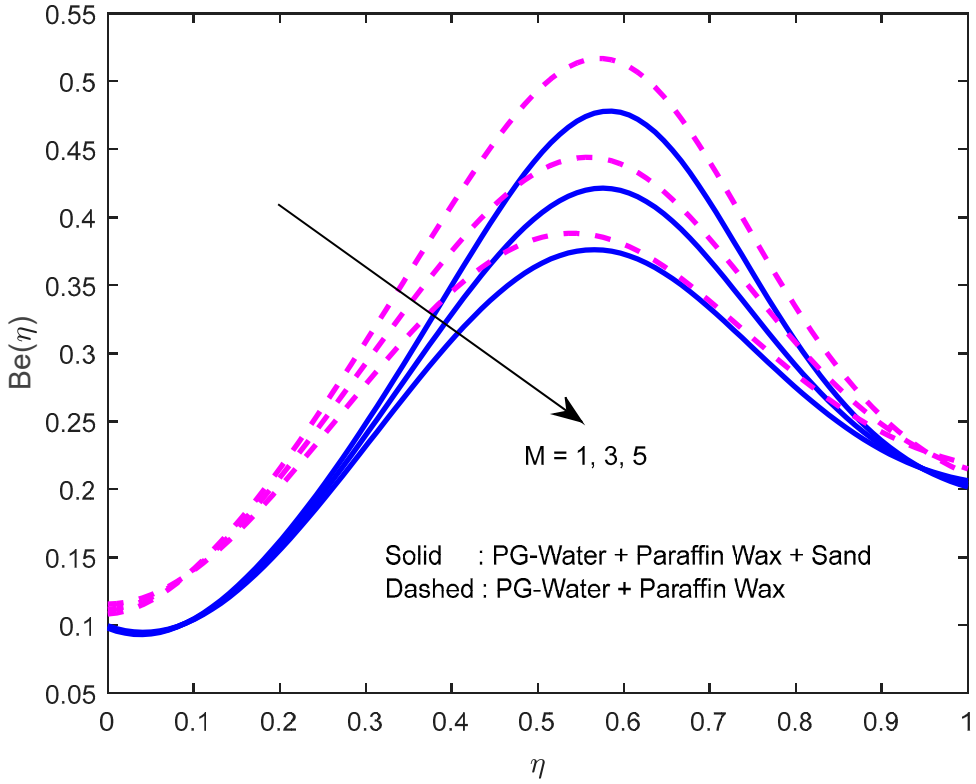

Figure 26. Effect of the magnetic field parameter on Bejan number profile.

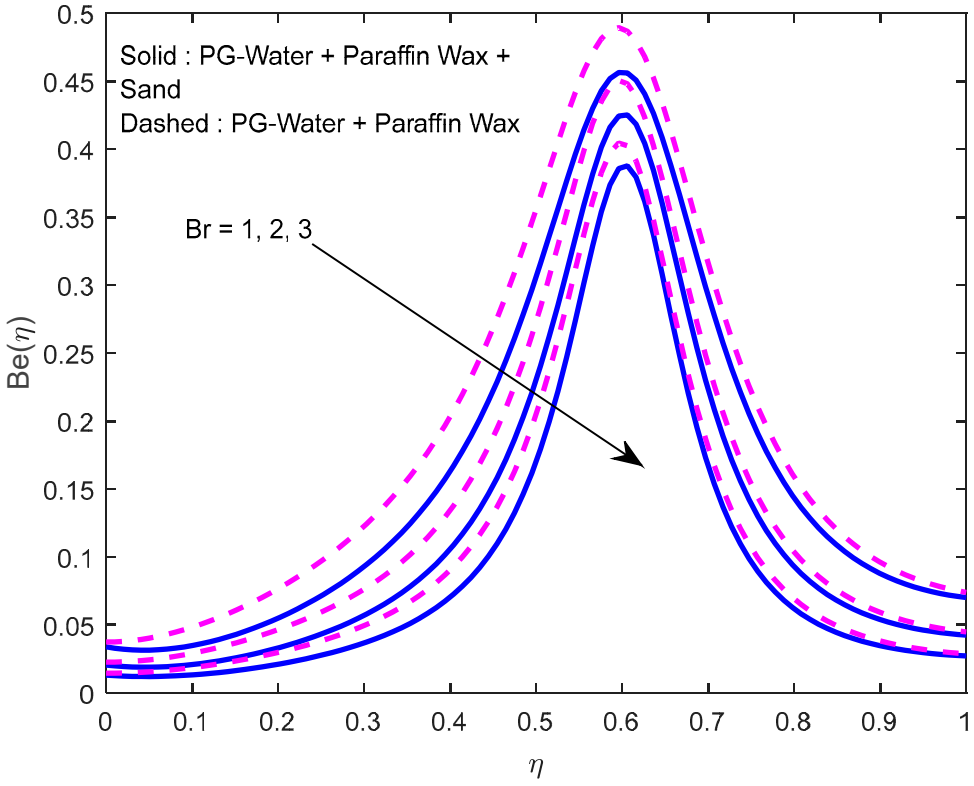

Figure 27. Effect of the Brinkmann number on Bejan number profile.

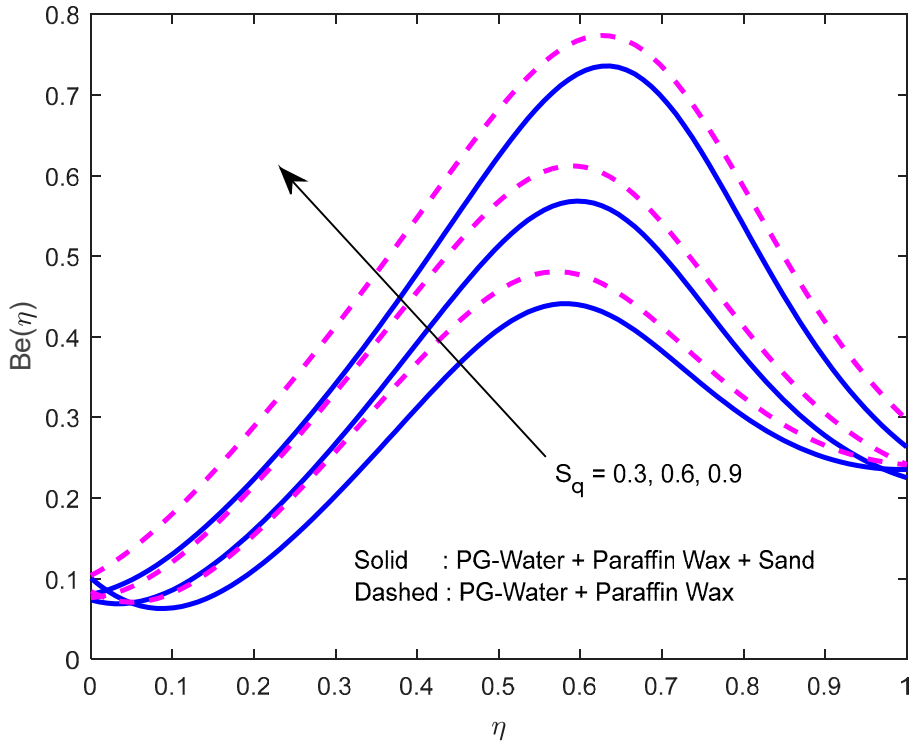

Figure 28. Effect of the squeeze number on Bejan number profile.

6. Conclusions

A hybrid nanofluid, which is a combination of a propylene glycol–water mixture and paraffin wax–sand, may be utilized as a standby for a propylene glycol–water blend in the solar thermal systems. In addition, the squeezing nanofluid flow has applications in different fields, such as chemical engineering, the food industry, and polymer preparation. Therefore, this study investigates the squeezing flow of a propylene glycol and water mixture-based hybrid nanofluid between two parallel plates with activation energy and entropy generation. A shooting strategy is applied to unravel converted equations. Results and related parameters relationships are demonstrated in graphs and discussed. In addition, the study uses a statistical tool (correlation coefficient) to elucidate the impact of pertinent parameters on the concern parameters, such as the surface friction factor at both plates. Furthermore, the study results verify the available data from the literature, and show good agreement.

The primary conclusions of the current investigation are listed below:

- A larger squeezing number intensifies velocity profiles;
- A raise in the rotation parameter deprecates the normal velocity (in the x-direction) in the lower half, and ameliorates it the same in the upper half;
- An escalation in fluid temperature is recognized with larger N;
- Fluid concentration reduces with higher reaction rate parameters, and raises with melioration in activation energy;
- The magnetic field, rotation parameter, and nanoparticle volumetric parameter have a strong negative relationship with the friction factor at the lower plate;
- The squeezing number escalates the friction factor near the lower plate, and depreciates it near the upper plate. N has a strong negative relationship with the heat transfer rate near the lower plate, and a strong positive correlation with the same phenomena near the upper plate;
- The Sherwood number minifies with larger Sc, Γ, α_1, and intensifies with larger E_n near the lower plate.

Author Contributions: All authors contributed to writing, reviewing, and editing of this manuscript. All authors have read and agreed to the published version of the manuscript.

Funding: This research received no external funding.

Data Availability Statement: The manuscript has no associated data.

Conflicts of Interest: The authors declare no conflict of interest.

Nomenclature

Nomenclature	
$B(t)$	Magnetic field (Tesla)
Be	Bejan number
Br	Brinkman number
C	Hybrid nanofluid concentration
C_p	Specific heat (J/kg K)
D_m	Molecular diffusivity
E_a	Activation energy
E_n	Activation energy parameter
f	Dimensionless axial velocity
g	Dimensionless transverse velocity
$H*$	Diffusion parameter
k	Thermal conductivity (W/m K)
$k*$	Mean absorption coefficient (1/m)
k_1	Boltzmann constant (J/K)
k_r	Chemical reaction rate (1/s)
M	Magnetic field parameter
N	Heat source parameter
n	Fitted rate constant
N_{EG}	Entropy generation
Nu_x	Nusselt number
p	Pressure
Pr	Prandtl number
q_w	Wall heat flux
Q_0	Dimensional heat source parameter (W/m^3K)
$\overline{R}$	Universal gas constant
R_a	Radiation parameter
V_0	Permeability parameter
S	Suction parameter
s_w	Wall mass flux
Sc	Schmidt number
S_q	Squeeze number
T	Fluid temperature (K)
u, v, w	Velocity component along x, y, and z-directions (m/s)
V_h	Squeezing velocity (m/s)
a	Stretching rate of lower plate

Greek Symbols	
α_1	Temperature difference parameter
α_2	Concentration ratio parameter
Γ	Reaction rate parameter
γ	Characteristic parameter with dimension of time^{-1}
η	Similarity variable
θ	Dimensionless temperature
μ	Dynamic viscosity (kg/m·s)
υ	Kinematic viscosity (m^2/s)
ρ	Density (kg/m^3)
ρC_p	Fluid heat capacity (J/Km^3)
σ	Electrical conductivity (S/m)
$\sigma*$	Stefan–Boltzmann constant (W/m^2K^4)
Φ	Dimensionless nanoparticle concentration
ϕ	Nanoparticle volume fractions
Ω	Rotation parameter
$\Omega*$	Angular velocity (m^2/s)
ω	Rotational velocity (1/s)

Subscripts	
f	Fluid
nf	Mono nanofluid
hnf	Hybrid nanofluid
s	Nanomaterials

References

1. Engmann, J.; Servais, C.; Burbidge, A.S. Squeeze flow theory and applications to rheometry: A review. *J. Non-Newtonian Fluid Mech.* **2005**, *132*, 1–27. [CrossRef]
2. Su, X.; Yin, Y. Effects of an inclined magnetic field on the unsteady squeezing flow between parallel plates with suction/injection. *J. Magne. Magn. Mater.* **2019**, *484*, 266–271. [CrossRef]
3. Munawar, S.; Mehmood, A.; Ali, A. Three-dimensional squeezing flow in a rotating channel of lower stretching porous wall. *Compu. Mathem. Applic.* **2012**, *64*, 1575–1586. [CrossRef]
4. Shahmohamadi, H.; Rashidi, M.M. VIM solution of squeezing MHD nanofluid flow in a rotating channel with lower stretching porous surface. *Advan. Powder Tech.* **2016**, *27*, 171–178. [CrossRef]

5. Hayat, T.; Tamoor, M.; Khan, M.I.; Alsaedi, A. Numerical simulation for nonlinear radiative flow by convective cylinder. *Results Phys.* **2016**, *6*, 1031–1035. [CrossRef]
6. Khan, U.; Ahmed, N.; Mohyud-Din, S.T. Numerical investigation for three dimensional squeezing flow of nanofluid in a rotating channel with lower stretching wall suspended by carbon nanotubes. *Appl. Ther. Eng.* **2017**, *113*, 1107–1117. [CrossRef]
7. Ahmad, S.; Hayat, T.; Alsaedi, A.; Khan, Z.H.; Khan, M.W.A. Finite difference analysis of time-dependent viscous nanofluid flow between parallel plates. *Commun. Theo. Phys.* **2019**, *71*, 1293. [CrossRef]
8. Al-Kouz, W.G.; Kiwan, S.; Alkhalidi, A.; Sari, M.E.; Alshare, A. Numerical study of heat transfer enhancement for low-pressure flows in a square cavity with two fins attached to the hot wall using Al_2O_3-air nanofluid. *Stroj. Vestn. J. Mech. Eng.* **2018**, *64*, 26–36.
9. Al-Kouz, W.; Al-Waked, R.; Sari, M.E.; Owhaib, W.; Atieh, A. Numerical study of heat transfer enhancement in the entrance region for low-pressure gaseous laminar pipe flows using Al_2O_3–air nanofluid. *Adv. Mech. Eng.* **2018**, *10*, 1687814018784410. [CrossRef]
10. Al-Kouz, W.; Al-Muhtady, A.; Owhaib, W.; Al-Dahidi, S.; Hader, M.; Abu-Alghanam, R. Entropy generation optimization for rarified nanofluid flows in a square cavity with two fins at the hot wall. *Entropy* **2019**, *21*, 103. [CrossRef]
11. Mahanthesh, B.; Mackolil, J.; Radhika, M.; Al-Kouz, W. Significance of quadratic thermal radiation and quadratic convection on boundary layer two-phase flow of a dusty nanoliquid past a vertical plate. *Int. Comm. Heat Mass Trans.* **2021**, *120*, 105029. [CrossRef]
12. Alshare, A.; Al-Kouz, W.; Alkhalidi, A.; Kiwan, S.; Chamkha, A. Periodically fully developed nanofluid transport through a wavy module. *J. Therm. Anal. Calor.* **2021**, *144*, 779–791. [CrossRef]
13. Owhaib, W.; Basavarajappa, M.; Al-Kouz, W. Radiation effects on 3D rotating flow of Cu-water nanoliquid with viscous heating and prescribed heat flux using modified Buongiorno model. *Sci. Rep.* **2021**, *11*, 20669. [CrossRef] [PubMed]
14. Al-Kouz, W.; Owhaib, W. Numerical analysis of Casson nanofluid three-dimensional flow over a rotating frame exposed to a prescribed heat flux with viscous heating. *Sci. Rep.* **2022**, *12*, 4256. [CrossRef] [PubMed]
15. Atlas, M.; Hussain, S.; Sagheer, M. Entropy generation and unsteady Casson fluid flow squeezing between two parallel plates subject to Cattaneo-Christov heat and mass flux. *Eur. Phys. J. Plus* **2019**, *134*, 33. [CrossRef]
16. Tarakaramu, N.; Satya Narayana, P.V. Chemical reaction effects on bio-convection nanofluid flow between two parallel plates in rotating system with variable viscosity: A numerical study. *J. Appl. Compu. Mech.* **2019**, *5*, 791–803.
17. Alzahrani, A.K.; Ullah, M.Z.; Muhammad, T. Numerical treatment for 3D squeezed flow in a rotating channel with Soret and Dufour effects. *Front. Phys.* **2022**, *8*, 201. [CrossRef]
18. Khan, M.I.; Qayyum, S.S.; Kadry, S.; Khan, W.A.; Abbas, S.Z. Irreversibility analysis and heat transport in squeezing nanoliquid flow of non-Newtonian (second-grade) fluid between infinite plates with activation energy. *Arab. J. Sci. Eng.* **2020**, *45*, 4939–4947. [CrossRef]
19. Upreti, H.; Pandey, A.K.; Kumar, M. Unsteady squeezing flow of magnetic hybrid nanofluids within parallel plates and entropy generation. *Heat Transf.* **2021**, *50*, 105–125. [CrossRef]
20. Zangooee, M.R.; Hosseini, S.A.; Ganji, D.D. Squeezing nanofluid flow between parallel rotating plates analysis by AGM method. *Int. J. Ambient Energy* **2020**, 1–8. [CrossRef]
21. Salehi, S.; Nori, A.; Hosseinzadeh, K.; Ganji, D.D. Hydrothermal analysis of MHD squeezing mixture fluid suspended by hybrid nanoparticles between two parallel plates. *Case Stud. Ther. Eng.* **2020**, *21*, 100650. [CrossRef]
22. Awan, S.E.; Raja, M.A.Z.; Gul, F.; Khan, Z.A.; Mehmood, A.; Shoaib, M. Numerical Computing Paradigm for Investigation of Micropolar Nanofluid Flow Between Parallel Plates System with Impact of Electrical MHD and Hall Current. *Arab. J. Sci. Eng.* **2021**, *46*, 645–662. [CrossRef]
23. Shankar, U.; Naduvinamani, N.B.; Basha, H. A generalized perspective of Fourier and Fick's laws: Magnetized effects of Cattaneo-Christov models on transient nanofluid flow between two parallel plates with Brownian motion and thermophoresis. *Nonlinear Eng.* **2020**, *9*, 201–222. [CrossRef]
24. Magodora, M.; Mondal, H.; Sibanda, P. Effect of Cattaneo-Christov heat flux on radiative hydromagnetic nanofluid flow between parallel plates using spectral quasilinearization method. *J. Appl. Compu. Mech.* **2022**, *8*, 865–875.
25. Mollah, M.T.; Poddar, S.; Islam, M.M.; Alam, M.M. Non-isothermal Bingham fluid flow between two horizontal parallel plates with Ion-slip and Hall currents. *SN Appl. Sci.* **2021**, *3*, 115. [CrossRef]
26. Babu, J.R.; Kumar, K.K.; Rao, S.S. State-of-art review on hybrid nanofluids. *Renew. Sust. Energ. Rev.* **2017**, *77*, 551–565. [CrossRef]
27. Hayat, T.; Ahmad, S.; Khan, M.I.; Alsaedi, A. Simulation of ferromagnetic nanomaterial flow of Maxwell fluid. *Results Phys.* **2018**, *8*, 34–40. [CrossRef]
28. Chen, X.; Wu, D.; Zhou, P.; Chen, M.; Yan, H. Modeling the solar absorption performance of Copper@ Carbon core–shell nanoparticles. *J. Mater. Sci.* **2021**, *56*, 13659–13672. [CrossRef]
29. Chen, X.; Xiong, Z.; Chen, M.; Zhou, P. Ultra-stable carbon quantum dot nanofluids for direct absorption solar collectors. *Sol. Energy Mater. Sol. Cells* **2022**, *240*, 111720. [CrossRef]
30. Qayyum, S.; Khan, M.I.; Hayat, T.; Alsaedi, A. Comparative investigation of five nanoparticles in flow of viscous fluid with Joule heating and slip due to rotating disk. *Phys. B Cond. Matter* **2018**, *534*, 173–183. [CrossRef]
31. Waini, I.; Ishak, A.; Pop, I. Hybrid nanofluid flow and heat transfer past a vertical thin needle with prescribed surface heat flux. *Int. J. Num. Methods Heat Fluid Flow* **2019**, *29*, 4875–4894. [CrossRef]

32. Maskeen, M.M.; Zeeshan, A.; Mehmood, O.U.; Hassan, M. Heat transfer enhancement in hydromagnetic alumina–copper/water hybrid nanofluid flow over a stretching cylinder. *J. Therm. Anal.* **2019**, *138*, 1127–1136. [CrossRef]
33. Khashi'ie, N.S.; Arifin, N.; Pop, I.; Nazar, R.; Hafidzuddin, E.H.; Wahi, N. Flow and heat transfer past a permeable power-law deformable plate with orthogonal shear in a hybrid nanofluid. *Alex. Eng. J.* **2020**, *59*, 1869–1879. [CrossRef]
34. Venkateswarlu, B.; Satya Narayana, P.V. Hybrid nanofluid flow past a porous stretching sheet due to temperatue-dependent viscosity and viscous dissipation. *Heat Transf.* **2021**, *50*, 432–449. [CrossRef]
35. Khan, M.I.; Alzahrani, F.; Hobiny, A.; Ali, Z. Modeling of Cattaneo-Christov double diffusions (CCDD) in Williamson nanomaterial slip flow subject to porous medium. *J. Mater. Res. Technol.* **2020**, *9*, 6172–6177. [CrossRef]
36. Acharya, N.; Bag, R.; Kundu, P.K. Influence of Hall current on radiative nanofluid flow over a spinning disk: A hybrid approach. *Phys. E Low-Dimens. Syst. Nanostruc.* **2019**, *111*, 103–112. [CrossRef]
37. Eid, M.R.; Nafe, M.A. Thermal conductivity variation and heat generation effects on magneto-hybrid nanofluid flow in a porous medium with slip condition. *Waves Random Complex Media* **2022**, *32*, 1103–1127. [CrossRef]
38. Khan, M.I.; Alzahrani, F.; Hobiny, A. Simulation and modeling of second order velocity slip flow of micropolar ferrofluid with Darcy–Forchheimer porous medium. *J. Mater. Res. Technol.* **2020**, *9*, 7335–7340. [CrossRef]
39. Abbas, N.; Malik, M.Y.; Nadeem, S.; Alarifi, I.M. On extended version of Yamada–Ota and Xue models of hybrid nanofluid on moving needle. *Euro. Phys. J. Plus* **2020**, *135*, 145. [CrossRef]
40. Ahmad, S.; Nadeem, S. Cattaneo–Christov-based study of SWCNT–MWCNT/EG Casson hybrid nanofluid flow past a lubricated surface with entropy generation. *Appl. Nanosci.* **2020**, *10*, 5449–5458. [CrossRef]
41. Jamshed, W.; Nisar, K.S. Single phase based study of Ag-Cu/EO Williamson hybrid nanofluid flow over a stretching surface with shape factor. *Phys. Scr.* **2021**, *96*, 065202. [CrossRef]
42. Reddy, M.G.; Kumar, N.; Prasannakumara, B.C.; Rudraswamy, N.G.; Kumar, K.G. Magnetohydrodynamic flow and heat transfer of a hybrid nanofluid over a rotating disk by considering Arrhenius energy. *Commun. Theor. Phys.* **2021**, *73*, 045002. [CrossRef]
43. Roy, N.C.; Hossain, M.; Pop, I. Analysis of Dual Solutions of Unsteady Micropolar HybridNanofluid Flow over a Stretching/Shrinking Sheet. *J. Appl. Comput. Mech.* **2021**, *7*, 19–33.
44. Menzinger, M.; Wolfgang, R. The meaning and use of the Arrhenius activation energy. *Angew. Chem. Intern. Ed. Eng.* **1969**, *8*, 438–444. [CrossRef]
45. Khan, M.I.; Hayat, T.; Waqas, M.; Alsaedi, A. Outcome for chemically reactive aspect in flow of tangent hyperbolic material. *J. Mol. Liq.* **2017**, *230*, 143–151. [CrossRef]
46. Devi, S.S.U.; Mabood, F. Entropy anatomization on Marangoni Maxwell fluid over a rotating disk with nonlinear radiative flux and Arrhenius activation energy. *Int. Commun. Heat Mass Transf.* **2020**, *118*, 104857. [CrossRef]
47. Kumar, K.G.; Baslem, A.; Prasannakumara, B.C.; Majdoubi, J.; Rahimi-Gorji, M.; Nadeem, S. Significance of Arrhenius activation energy in flow and heat transfer of tangent hyperbolic fluid with zero mass flux condition. *Microsyst. Technol.* **2020**, *26*, 2517–2526. [CrossRef]
48. Bhatti, M.M.; Michaelides, E.E. Study of Arrhenius activation energy on the thermo-bioconvection nanofluid flow over a Riga plate. *J. Therm. Anal.* **2021**, *143*, 2029–2038. [CrossRef]
49. Khan, M.I.; Alzahrani, F. Binary chemical reaction with activation energy in dissipative flow of non-Newtonian nanomaterial. *J. Theor. Comput. Chem.* **2020**, *19*, 2040006. [CrossRef]
50. Irfan, M.; Anwar, M.S.; Rashid, M.; Waqas, M.; Khan, W.A. Arrhenius activation energy aspects in mixed convection Carreau nanofluid with nonlinear thermal radiation. *Appl. Nanosci.* **2020**, *10*, 4403–4413. [CrossRef]
51. Wang, J.; Khan, M.I.; Khan, W.A.; Abbas, S.Z.; Khan, M.I. Transportation of heat generation/absorption and radiative heat flux in homogeneous–heterogeneous catalytic reactions of non-Newtonian fluid (Oldroyd-B model). *Comp. Methods Programs Biomed.* **2020**, *189*, 105310. [CrossRef] [PubMed]
52. Salawu, S.O.; Fatunmbi, E.O.; Okoya, S.S. MHD heat and mass transport of Maxwell Arrhenius kinetic nanofluid flow over stretching surface with nonlinear variable properties. *Results Chem.* **2021**, *3*, 100125. [CrossRef]
53. Jawad, M.; Saeed, A.; Gul, T.; Bariq, A. MHD Darcy-Forchheimer flow of Casson nanofluid due to a rotating disk with thermal radiation and Arrhenius activation energy. *J. Phys. Commun.* **2021**, *5*, 025008. [CrossRef]
54. Muhammad, T.; Waqas, H.; Khan, S.A.; Ellahi, R.; Sait, S.M. Significance of nonlinear thermal radiation in 3D Eyring–Powell nanofluid flow with Arrhenius activation energy. *J. Ther. Anal.* **2021**, *143*, 929–944. [CrossRef]
55. Kotresh, M.J.; Ramesh, G.K.; Shashikala, V.K.R.; Prasannakumara, B.C. Assessment of Arrhenius activation energy in stretched flow of nanofluid over a rotating disc. *Heat Transf.* **2021**, *50*, 2807–2828. [CrossRef]
56. Childs, P.R. *Rotating Flow*; Elsevier: Amsterdam, The Netherlands, 2011; ISBN 978-0-12-382098-3.
57. Hayat, T.; Nadeem, S.; Khan, A.U. Rotating flow of Ag-CuO/H_2O hybrid nanofluid with radiation and partial slip boundary effects. *Eur. Phys. J. E* **2018**, *41*, 75. [CrossRef]
58. Shoaib, M.; Raja, M.A.Z.; Sabir, M.T.; Islam, S.; Shah, Z.; Kumam, P.; Alrabaiah, H. Numerical investigation for rotating flow of MHD hybrid nanofluid with thermal radiation over a stretching sheet. *Sci. Rep.* **2020**, *10*, 18533. [CrossRef]
59. Lei, T.; Siddique, I.; Ashraf, M.K.; Hussain, S.; Abdal, S.; Ali, B. Computational analysis of rotating flow of hybrid nanofluid over a stretching surface. *Proc. Inst. Mech. Eng. Part E J. Process. Mech. Eng.* **2022**, 09544089221100092. [CrossRef]
60. Mohd Sohut, N.F.H.; Soid, S.K.; Abu Bakar, S.; Ishak, A. Unsteady Three-Dimensional Flow in a Rotating Hybrid Nanofluid over a Stretching Sheet. *Mathematics* **2022**, *10*, 348. [CrossRef]

61. Mukhtar, T.; Jamshed, W.; Aziz, A.; Al-Kouz, W. Computational investigation of heat transfer in a flow subjected to magnetohydrodynamic of Maxwell nanofluid over a stretched flat sheet with thermal radiation. *Numer. Methods Partial. Differ. Equ.* **2020**. [CrossRef]
62. Gatsonis, N.A.; Al-Kouz, W.G.; Chamberlin, R.E. Investigation of rarefied supersonic flows into rectangular nanochannels using a three-dimensional direct simulation Monte Carlo method. *Phys. Fluids* **2010**, *22*, 032001. [CrossRef]
63. Amine, B.M.; Redouane, F.; Mourad, L.; Jamshed, W.; Eid, M.R.; Al-Kouz, W. Magnetohydrodynamics natural convection of a triangular cavity involving Ag-MgO/water hybrid nanofluid and provided with rotating circular barrier and a quarter circular porous medium at its right-angled corner. *Arab. J. Sci. Eng.* **2021**, *46*, 12573–12597. [CrossRef]
64. Anantha Kumar, K.; Sugunamma, V.; Sandeep, N. Effect of thermal radiation on MHD Casson fluid flow over an exponentially stretching curved sheet. *J. Therm. Anal. Calorim.* **2020**, *140*, 2377–2385. [CrossRef]
65. Manikandan, S.; Rajan, K.S. New hybrid nanofluid containing encapsulated paraffin wax and sand nanoparticles in propylene glycol-water mixture: Potential heat transfer fluid for energy management. *Energy Convers. Manag.* **2017**, *137*, 74–85. [CrossRef]
66. Khan, M.I.; Rahman, M.U.; Khan, S.A.; Hayat, T.; Khan, M.I. Evaluation of entropy generation in cubic autocatalytic unsteady squeezing flow of nanofluid between two parallel plates. *Comput. Methods Programs Biomed.* **2020**, *185*, 105149. [CrossRef]